Space Sci Rev (2021) 217:36
https://doi.org/10.1007/s11214-021-00791-1

Do Intrinsic Magnetic Fields Protect Planetary Atmospheres from Stellar Winds?

Lessons from Ion Measurements at Mars, Venus, and Earth

Robin Ramstad[1] · **Stas Barabash**[2]

Received: 10 December 2019 / Accepted: 6 January 2021 / Published online: 9 March 2021

Abstract The accumulation of detailed ion flux measurements from long-lived spacecraft orbiting the solar system's terrestrial planets have enabled recent studies to estimate the rate of solar wind driven atmospheric ion escape from Venus, Earth, and Mars, as well as the influence of solar wind and solar extreme ultraviolet (EUV) ionizing radiation on the atmospheric ion escape rates. Here, we introduce the basic forces and processes of ion escape, review the recent studies of ion escape rates, and provide a general framework for understanding ion escape as a process that can be limited by potential bottlenecks, such as ion supply, solar wind energy transfer, and transport efficiency, effectively determining the state of the ion escape process at each planet. We find that ion escape from Venus and Earth is energy-limited, though exhibit different dependencies on solar wind and EUV, revealing the influence of Earth's intrinsic magnetic field. In contrast, ion escape from Mars is in a supply-limited state, mainly due to its low gravity, and has likely contributed relatively little to the total loss of the early Martian atmosphere, in comparison to neutral escape processes. Contrary to the current paradigm, the comparisons between the solar system planets show that an intrinsic magnetic dipole field is not required to prevent stellar wind-driven escape of planetary atmospheres, and the presence of one may instead increase the rate of ion escape. Anticipating the atmospheres of the exoplanets that will begin to be characterized over the coming decade, and the need to explain their evolution, we argue that a modern, nuanced, and evidence-based view of the magnetic field's role in atmospheric escape is required.

Keywords Magnetosphere · Atmospheric escape · Stellar wind

Understanding the Diversity of Planetary Atmospheres
Edited by François Forget, Oleg Korablev, Julia Venturini, Takeshi Imamura, Helmut Lammer and Michel Blanc

✉ R. Ramstad
robin.ramstad@lasp.colorado.edu

[1] Laboratory for Atmospheric and Space Physics, University of Colorado, Boulder, USA

[2] Swedish Institute of Space Physics, Kiruna, Sweden

1 Introduction

Starting in the coming decade, advances in exoplanet observations are expected to elucidate a wide range of atmospheres bound to planets outside the solar system. The task to explain the evolutionary paths that led to these atmospheres will be daunting, particularly if we consider the lasting difficulties in reconciling the divergent evolution of the atmospheric terrestrial planets in the solar system; Venus, Earth, and Mars. All three are thought to have formed with similar early atmospheres, which evolved towards their drastically different present-day conditions. This fundamental planetological problem persists despite decades of visits by spacecraft, providing in situ and remote measurements by orbiters and landers. Yet, these kinds of observations will not be available to exoplanet researchers, who will have to rely on remote measurements for the foreseeable future. How confident will we then be in our interpretations of planets around other stars if we cannot conclusively determine the evolution of the planetary atmospheres in our backyard? How did Venus' atmosphere end up with 92 bars, Earth's with 1 bar, and Mars' with only about 6.4 mbar?

Unlike on Earth and Venus, the lack of tectonic activity and recent volcanism on Mars has preserved intricate and widespread fluvial patterns on a wide range of scales, and thus also the clear geological evidence for an active hydrological cycle sustained through a strong greenhouse effect created by a thick atmosphere 3.3–4.2 Ga ago (Mangold et al. 2016). Specifically, a CO_2-dominated early Martian atmosphere would have required a surface pressure of 0.5–3.0 bar (depending on other constituents) to prevent greenhouse collapse (Ramirez et al. 2014; Ramirez 2017; Wordsworth et al. 2017). In addition, a $\gtrsim$100 m global equivalent water layer has since been removed from the planet's volatile inventory as indicated by the elevated atmospheric D/H-ratio (Villanueva et al. 2015). While hydrogen escapes thermally from Mars upper atmosphere as H and H_2 from dissociated H_2O, the left-over oxygen and CO_2 remain gravitationally bound to the planet even at the highest estimated exobase temperatures ($\sim$300 K). If the amount of carbon sequestered in the ground is only equivalent to 12 mbar as current estimates indicate (Edwards and Ehlmann 2015), another effective superthermal escape mechanism is necessary to explain the removal of atmosphere on the order of a bar, to yield the presently remaining pressure of $\sim$6 mbar. As we will discuss in Sect. 5.2, there are exothermic photochemical reactions that facilitate significant escape of neutral oxygen from Mars (though not from Earth or Venus). Nevertheless, the most common hypothesis for the loss of the early Martian atmosphere suggests that the absence of an global Martian magnetic dipole has allowed the solar wind to interact closely with the Martian ionosphere, in the process effectively transferring energy and momentum, driving bulk atmospheric ion escape.

Ion escape is to one degree or another an active process wherever the solar wind interacts with an atmospheric body. In particular, the lack of a global Martian magnetic dipole appears to provide a satisfying explanation for why the Martian atmosphere is tenuous, and has been considered as such for a long time. According to this hypothesis, Earth's atmosphere has been protected by the geomagnetic field, which deflects the solar wind at a distance of several Earth radii. Protection against strong solar winds is particularly important for atmospheric stability, as the solar wind was many times more energetic in the past (Wood 2006). However, Venus does not appear to fit well in this explanation, having retained its also CO_2-dominated 92 bar atmosphere without any discernible intrinsic magnetic field, despite an orbit closer to the Sun, where Venus is subjected to solar wind and solar ionizing radiation about twice as intense as at Earth, and about four times the intensity at Mars. This apparent incongruence implies the need for an explanation that considers other intrinsic differences between the planets, in particular the weak gravity of Mars, compared to Venus and Earth.

The accumulation of large sets of ion flux measurements from long-lived orbiters, such as Cluster (2001–present), Mars Express (2004–present), the Mars Atmosphere and Volatile EvolutioN (MAVEN) mission (2014–present), and Venus Express (2006–2014), are enabling detailed empirical studies of atmospheric ion escape and its driving factors. In the following sections we review and compare the results from each planet and discuss what the observed escape rates and varied dependencies on upstream conditions reveal about the influence of planetary properties, such as intrinsic magnetism and gravity, on the interaction with the solar wind and the associated atmospheric loss. While Earth, Mars and Venus together only constitute three datapoints in a large parameter space of possible planetary properties, the range of varying upstream conditions may inform our understanding of ion escape as a general process, aiding our understanding of the evolution of planetary atmospheres also outside the solar system.

2 Ion Escape in Induced and Intrinsic Magnetospheres

2.1 General Physics of Ion Escape

The solar wind is a stream of highly ionized plasma driven by the expansion of the solar corona throughout interplanetary space, and is naturally the most well-studied of stellar winds. The coronal plasma at the source region near the Sun is highly magnetized due to the strong magnetic fields originating from the Solar interior, and the currents that connect the Sun to the rest of the solar system. As noted by Alfvén (1957) and Parker (1958), the magnetic fields are thus "frozen in" the expanding plasma, forming the Interplanetary Magnetic Field (IMF). The rotation of the Sun and expansion of the solar wind together gives the IMF a spiral-like shape, i.e. the Parker spiral.

In the frozen-in condition, currents ($\mathbf{J}$) and charge polarization gradients (∇p_e) are small, thus the electric field ($\mathbf{E}$) of the solar wind, as given by the generalized Ohm's law

$$\mathbf{E} = -\mathbf{v} \times \mathbf{B} + \frac{1}{n_e e}\mathbf{J} \times \mathbf{B} - \frac{1}{n_e e}\nabla p_e + \mathbf{J}/\sigma, \tag{1}$$

is dominated by the motional component,

$$\mathbf{E}_{\text{mot}} = -\mathbf{v}_{\text{sw}} \times \mathbf{B}_{\text{IMF}}. \tag{2}$$

Here, $\mathbf{E}_{\text{mot}}$ is the motional electric field of the solar wind, $\mathbf{v}_{\text{sw}}$ is the solar wind velocity, and $\mathbf{B}_{\text{IMF}}$ is the local interplanetary magnetic field. In the reference frame co-moving with the solar wind the motional electric field is zero, thus the solar wind particles gyrate without energization from the bulk motion. However, in a reference frame fixed on an obstacle to the solar wind the motional electric field is non-zero and responsible for directly or indirectly transferring energy and momentum to the obstacle. In the case of an atmospheric body, this energy can power Joule heating of conductive layers of the upper atmospheres (through the $\mathbf{J}/\sigma$ resistive term in Eq. (1), where σ is the conductivity), and the non-thermal escape of atmospheric ions (here with charge q) through acceleration by the Lorentz force,

$$\mathbf{F} = q(\mathbf{E} + \mathbf{v} \times \mathbf{B}). \tag{3}$$

In order to escape the planet's gravity, the ion has to gain a velocity higher than the planet's escape velocity, which equates to a mass-dependent minimum escape energy,

$$E_{\text{esc}} = m\frac{GM_p}{r_0}, \tag{4}$$

Table 1 Escape velocities and energies at the respective exobase altitudes of Venus, Earth, and Mars

Planet	Escape velocity	Escape energy		
		H^+	O^+	O_2^+
Venus	10.2 km/s	0.54 eV	8.6 eV	17.2 eV
Earth	10.6 km/s	0.59 eV	9.3 eV	18.7 eV
Mars	4.9 km/s	0.12 eV	2.0 eV	4.0 eV

where m is the mass of the particle, G is the gravitational constant, M_p is the mass of the planet, and r_0 is the distance from the planet's center. The escape energies for common ion species at Venus, Earth, and Mars are listed in Table 1 for reference, we can see that ion escape from Venus and Earth requires over 4 times the kinetic energy to escape from Mars. Consequently, as we explore in this paper, ion escape from Mars operates under intrinsically different conditions compared to both Earth and Venus, despite the similar non-magnetized state of the latter.

In contrast to neutral escape processes, which solely rely on the properties and processes near the exobase region, ions can be continuously energized as they reach higher altitudes. To escape, the ion needs to gain sufficient energy on a path to distant space, C, which is at least the escape energy, i.e.

$$\frac{m|v_0|^2}{2} + q\int_C (\mathbf{E}(\mathbf{r}) + \mathbf{v}(\mathbf{r}) \times \mathbf{B}(\mathbf{r})) \cdot d\mathbf{s} > E_{\text{esc}}. \tag{5}$$

Here, v_0 is the initial velocity inherited from the ionized neutral particle (equivalent to typical exobase thermal energies of about 0.02–0.1 eV), $\mathbf{r}$ is the position of the particle, and $d\mathbf{s}$ is an infinitesimal segment of C. Each of the electric field terms in equation (1) provides a mechanism for energization, and are often described as separate *escape channels* depending on which mechanism that dominates the resulting ion distribution.

2.2 In Induced Magnetospheres

Consider the introduction of a stationary neutral gas cloud in the solar wind flow, one sufficiently tenuous to be non-collisional with the solar wind. Solar EUV radiation will illuminate the cloud and ionize the neutral particles, producing photoions and photoelectrons, which are sensitive to the Lorentz force (equation (3)) as their constituent charges are non-zero, i.e. $q \neq 0$. Since $\mathbf{E}_{\text{mot}}$ is perpendicular to $\mathbf{v}_{\text{sw}}$, the initial motion of the photoions/electrons is perpendicular to the solar wind flow and the gyration around $\mathbf{B}_{\text{IMF}}$ leads to a cycloid trajectory with a gyrocenter drift velocity equal to the solar wind bulk velocity. The introduction of electrically sensitive mass from the photoion production in the solar wind flow is called mass-loading; the associated transfer of energy and momentum to the photoions, conversely, decelerates the solar wind and deflects it in the $-\mathbf{E}_{\text{mot}}$-direction.

The pick-up process is a comparatively energetic acceleration mechanism, typical magnitudes for $\mathbf{E}_{\text{mot}}$ in the inner solar system span 5 mV/m at Venus to 0.7 mV/m at Mars. A single-charged ($q = 1$ e) photoion produced in the undisturbed solar wind will thus, within a few km, reach energies of several eV at Mars and tens of eV at Venus, well above escape energy even for heavy ions such as O^+. At a quarter gyration, the speed of the pick-up ion in the initial rest frame will be up to twice that of the solar wind, by which point heavy pick-up ions can reach energies of a few 10,000's eV. However, the magnitude of $\mathbf{E}_{\text{mot}}$ is strongly controlled by the angle between $\mathbf{v}_{\text{sw}}$ and $\mathbf{B}_{\text{IMF}}$, which is not necessarily perpendicular, thus

ion pick-up can be responsible for a wide energization range, especially near a planet where the deflected solar wind flow can be near-parallel to the magnetic field.

Ion pick-up is active in the exospheres of induced magnetospheres, where the ion production rate is low enough to not significantly influence the bulk distribution of the solar wind. However, close to active comets and the upper atmospheres of Mars and Venus the photoion production rate is far higher. The mass-loading drives a pick-up current, enhancing the magnetic field (Phillips et al. 1987), in turn deflecting the solar wind. In the interaction with the solar wind, $\mathbf{E}_{\mathrm{mot}}$ generates a potential difference across the system, driving induced currents in conductive regions (Baumjohann et al. 2010; Ramstad et al. 2020), which in turn contribute to the strength of the magnetic barrier and a separation of the solar wind and ionospheric plasma domains.

The stand-off point of the solar wind and any magnetosphere occurs where the magnetic pressure balances the solar wind dynamic pressure. At an unmagnetized planet, the magnetic pressure is equivalent to the induced magnetic pressure (Dubinin et al. 2008), so that

$$\frac{B_{\mathrm{ind}}^2}{2\mu_0} = \frac{1}{2} n_{\mathrm{sw}} v_{\mathrm{sw}}^2 \cos^2(\theta_{\mathrm{inc}}), \tag{6}$$

where θ_{inc} is the local incidence angle of the solar wind on the boundary. This boundary is commonly named as either the Induced Magnetosphere Boundary (IMB) or the Magnetic Pile-up boundary (MPB), typically depending on the method of observation. Inside the magnetic barrier the atmospheric plasma is screened from direct pick-up by the solar wind, however, solar wind energy can still be transferred inside the barrier by the induced ionospheric direct currents (Saunders and Russell 1986), by magnetosonic waves (Fowler et al. 2018), by a small fraction of solar wind precipitating as charged particles (Diéval et al. 2013) and as Energetic Neutral Atoms (ENAs) (Halekas et al. 2015a), in addition to precipitating planetary pick-up ions energized by the solar wind (Hara et al. 2017). The currents driven by the magnetospheric electric fields impart a corresponding Hall force (the $\mathbf{J} \times \mathbf{B}$ term in equation (1)), which is particularly effective at accelerating charged particles in thin magnetic neutral sheets, where the conductivity is defined by gyroconductivity of the magnetized particle species (Lyons and Speiser 1985). In induced magnetospheres the neutral sheet is shaped by the draping of the IMF around the conductive obstacle (Riedler et al. 1989).

The rightmost term in equation (1), the ∇p_e (ambipolar) term, is determined by the distribution of charged particles along magnetic field lines. The large mass-difference between ions and electrons imply a proportionally large difference in the velocity distributions and thus spread of the two particle species in the gravitational field of the planet along the field line. The separation of ions and electrons is a departure from the quasi-neutrality and sets up a field-aligned polarization electric field. The ionospheres of non-magnetized planets can become magnetized, as is the typical case at Mars (Dubinin et al. 2008), and a response to high solar wind dynamic pressure at Venus (Russell et al. 1989). The ambipolar potential of Venus has been estimated as 9.9 ± 1.1 V on orbits where it is detectable (Collinson et al. 2016). In contrast, the Martian ionospheric ambipolar potential is at most 0.8 V (Akbari et al. 2019; Xu et al. 2018).

Ion escape channels in an induced magnetosphere are often divided into tail escape and pick-up escape, characterized by nightward ion outflow and solar wind scavenging of the dayside ionosphere (including direct pick-up of the photoions born in the solar wind flow), respectively. An illustration of the typical configuration of an induced magnetosphere and the approximate location of the dominating electric field term is shown in Fig. 1.

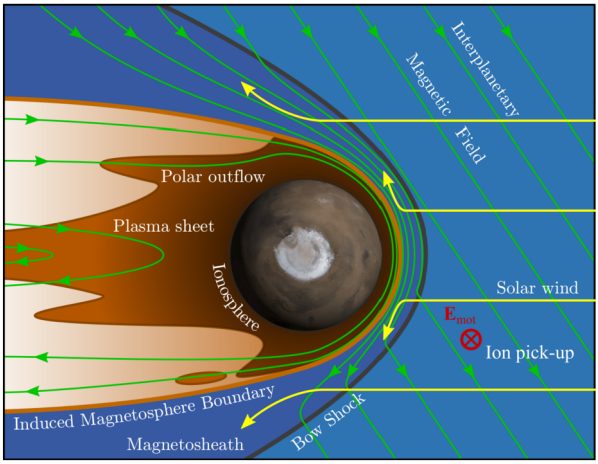

Fig. 1 Illustration of atmospheric ion escape in an induced magnetospheres. The ionosphere imposes a conductive obstacle to the solar wind, slowing and deflecting the solar wind due to the induced magnetic pressure, leading to the formation of the induced magnetosphere. Different ion energization channels dominate by location; charge-gradients (∇p_e) on open field-lines connected to the ionosphere drive polar ion outflow, currents that maintain the neutral plasma sheet energize ions through the $\mathbf{J} \times \mathbf{B}$-force, and exospheric ions produced in the solar wind are picked-up by the solar wind motional ($-\mathbf{v} \times \mathbf{B}$) electric field

2.3 In Intrinsic Magnetospheres

The same acceleration processes apply in intrinsic magnetospheres as in their induced counterparts. However, the presence of a strong intrinsic magnetic field alters the configuration of the forces involved in the interaction, and thus also the coupling with the solar wind. Since the magnetic pressure is no longer solely determined by the induced magnetic pressure, a strong magnetic field can stand off the solar wind far away from the planet, as is the case at the Earth and the outer planets.

The large distance between the solar wind and the Earth, separated by the intrinsic magnetosphere, often leads the magnetosphere to be described as Earth's "shield" against the solar wind. However, the interaction between the solar wind and the planetary magnetic field induces a large-scale magnetospheric convective electric field (Volland 1973), field-aligned, Pedersen, and Hall currents (Ganushkina et al. 2018), wave activity (Moore and Horwitz 2007; Nilsson et al. 2012a), and polarization electric fields (Yau et al. 2007) – all are processes that transfer some solar wind energy to the ionosphere, energizing atmospheric ions. In the cusps of the polar regions, the vertical field-lines thus provide a conduit for electrodynamic energy transfer between the solar wind and deep layers of the ionosphere, forming the auroral oval (Cowley 2000; Keiling et al. 2003). In addition, the field lines guide energized particles into the polar upper atmosphere, depositing more energy and providing an additional ion production process through electron-impact ionization, yielding more atmospheric particles sensitive to energization by electric fields (Strangeway et al. 2005).

Upon energization in the ionosphere, initially from a ∼2 V ambipolar potential (Fung and Hoffman 1991), an upwelling or outflowing ion may take any of a number of complex pathways in the magnetosphere, guided by the magnetic field lines. An illustration of these pathways is shown in Fig. 2, adapted from Seki et al. (2001). The ion may be further energized to a wide range of energies depending on which of the various regions of the magnetosphere it enters. Nevertheless, even if the ion is energized past escape energy, it

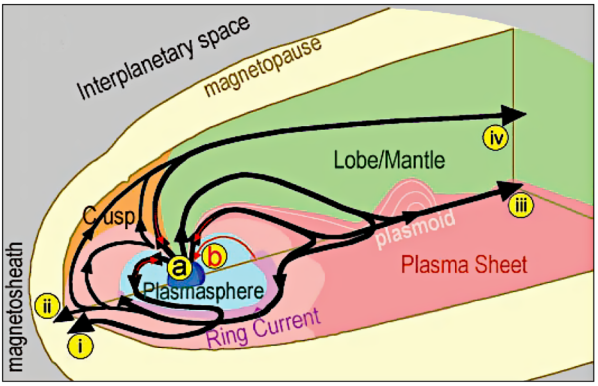

Fig. 2 Illustration of atmospheric ion escape in the Earth's intrinsic magnetosphere adapted from Seki et al. (2001). Black arrows show escaping paths and red arrows show returning/recycling paths. Ions originating in the polar ionosphere can escape directly downtail through the lobes (iv), by downstream acceleration in the plasma sheet (iii), from leaving the ring current (ii) or the plasmasphere (i) by crossing the magnetopause

may only escape if it is guided on open field lines or ejected on closed field lines in plasmoid ejection events (Kistler et al. 2010). Instead, an outflowing ion on a closed field line may be trapped in the plasmasphere, from which the ion may be returned to the upper atmosphere (recycled), unless the plasmasphere is disturbed and emptied. If the outflowing ion follows an open field-line it may be carried to the high altitude cusp, further energized and escape through the mantle or one of the tail lobes. Alternatively, the field line may border the neutral sheet, where the associated cross-tail current may accelerate the ion downtail, or a fast reconnection event may accelerate the ion back toward the planet. In the latter case the accelerated ion may follow a field-line back to the planet and be recycled, or drift around the planet in the dipole field. If the injected ion drift orbit is at least quasistable the ion will contribute to the ring current. However, if the dipole field is disturbed, the ring current may dissipate as the orbits become unstable, causing ions to either precipitate into the atmosphere or cross the magnetopause to be accelerated by the solar wind plasma in the mantle/magnetosheath.

Clearly, the pathways from ions being produced in the upper atmosphere, to their energization, and eventual transport to open space are complex. The processes involved are inextricably linked since magnetospheric processes can lead to precipitation of energetic particles which in turn produce more ions. The overall effect of the intrinsic magnetic field on the escape process is not obvious, and atmospheric escape from magnetospheres with other dipole strengths has not been studied in situ. Other dipole strengths can be explored e.g. with global magnetohydrodynamic (MHD) and hybrid (fluid-kinetic) models of the solar wind interaction, which capture many aspects of the escape process. Yet, even the most sophisticated models cannot simultaneously include the full range of physics (waves, realistic resistivities, reconnection), interconnected processes (Magnetosphere-Thermosphere-Ionosphere coupling), and spatio-temporal scales involved. Fortunately, several studies have estimated the ion escape rate from the Earth and its dependencies using measurements from orbiting spacecraft, thus careful comparisons with similar studies at Mars and Venus enables us to infer the overall effect of Earth's magnetic field among all other differences.

3 Measurements of Ion Escape from Earth, Mars and Venus

3.1 How Global Ion Escape Rates Are Measured

Orbiters have measured planetary ions in situ for decades, starting with the 1978 NASA/ESRO International Sun-Earth Explorer (ISEE) satellites at Earth, the 1978 NASA Pioneer Venus

Table 2 List of missions with suitable instrumentation to measure ion escape from Earth, Mars, and Venus, considered here

Mission	Plasma particle instrumentation	Spinner/stabilized	Planet	Duration
Phobos-2	Automatic Space Plasma Experiment with a Rotating Analyzer (ASPERA)	Spinner	Mars	Jan. – Mar. 1989
Akebono	Suprathermal ion Mass Spectrometer (SMS)	Spinner	Earth	1989-2015
Fast Auroral Snapshot Explorer (FAST)	Time-of-flight Energy Angle Mass Spectrograph (TEAMS)	Spinner	Earth	1996–2009
Cluster (×4)	Cluster Ion Spectrometry/COmposition and Distribution Function Analyzer (CIS/CODIF)	Spinners	Earth	2001–present
Mars Express (MEX)	Analyzer of Space Plasmas and Energetic Atoms/Ion Mass Analyzer (ASPERA-3/IMA)	3-axis stabilized	Mars	2004–present
Venus Express (VEX)	Analyzer of Space Plasmas and Energetic Atoms/Ion Mass Analyzer (ASPERA-4/IMA)	3-axis stabilized	Venus	2006–2014
Mars Atmosphere and Volatile EvolutioN (MAVEN)	SupraThermal and Thermal Ion Composition (STATIC)	3-axis stabilized	Mars	2014–present

Orbiter (PVO) at Venus, and the 1971–1973 Soviet Mars 2–5 missions. However, only relatively recently have orbiters returned data with sufficient quality and coverage to accurately quantify escape rates and the influence of upstream conditions. Here we will focus on results from seven missions and their respective scientific investigations, listed in Table 2.

In the purpose of understanding evolution of planetary atmospheres, the relevant studies generally focus on obtaining a global rate of atmospheric loss, i.e. the integrated net flux of particles over the full flow area. Plasma particle instruments on orbiting spacecraft natively measure differential flux, j, and cover some domain in the local velocity space by use of an electrostatic energy analyzer (ESA). The most common ESA ion-optical design in modern instruments is the top-hat, whereby incident ions are guided to the space between two spherical segments which are charged to different potentials, creating a static electric field in-between. The ion paths are deflected by the electric field along spherical trajectories, at a given field strength there is a corresponding ion energy-per-charge (E/q) that will follow a curvature matching a range of radii which let ion pass the space between the spheres. These are the only ions that will reach the opposite end of the ESA spherical segments where the ions can be counted. By sweeping the ESA voltage the instrument effectively samples the local ion energy distribution in all azimuthal directions simultaneously.

In this type of ESA there is a co-dependence between the ion entrance elevation angle and the acceptance energy. Therefore, to achieve a reasonable energy resolution ($\Delta E/E$) the range of entrance elevation angles must be kept small (usually $\sim 5°$). While ions can enter from any azimuthal direction (360°) the top-hat ESA thus has a narrow field-of-view (FOV), sampling a disk-shaped part of the local velocity space. To achieve 3D coverage in velocity space, some particle instruments are mounted on spinning spacecraft, e.g. Phobos-2/ASPERA (Lundin et al. 1985), FAST/TEAMS (Klumpar et al. 2001), and CLUSTER/CODIF (Rème et al. 2001). These instruments rely on spacecraft rotation to sweep the ESA FOV over the unit sphere with every half rotation, assuming the ESA FOV is

unobstructed. Instruments on 3-axis stabilized spacecraft cannot rely on rotation and instead use electrostatic deflectors to sweep the ESA entrance elevation angle, e.g. MEX/ASPERA-3 (Barabash et al. 2006), VEX/ASPERA-4 (Barabash et al. 2007a), as well as MAVEN's STATIC (McFadden et al. 2015) and Solar Wind Ion Analyzer (SWIA) instruments (Halekas et al. 2015b). While electrostatic deflectors are versatile and can provide high-cadence coverage of the distribution, the entrance angle is typically limited to $\pm 45^\circ$ from the ESA plane and may also see significant blockage by spacecraft surfaces. Therefore the FOV coverage of instruments on 3-axis stabilized spacecraft have to be carefully considered when analyzing the measured ion distributions.

All of the instruments mentioned above include mass-separation capabilities (except SWIA), which provides crucial information to understand atmospheric evolution as the escape of e.g. H^+, O^+ and CO_2^+ have mutually different implications, both in terms of composition, neutral source particle, and total mass rate of the atmospheric loss. The ions exiting the instrument ESAs are nearly monoenergetic (within the energy resolution of the ESA and for ions of equal charge), thus the velocity of the ions only varies depending on the mass per charge of the ion species. The mass-separation is subsequently performed using any of a variety of mechanisms. Phobos-2/ASPERA used a stepping Wien ($\mathbf{E} \times \mathbf{B}$) velocity filter, and an array of channel electron multipliers to detect the particles. MEX/ASPERA-3 and VEX/ASPERA-4 both employ a permanent magnet array in the respective IMA instruments that separates ions of different gyroradii (and thus mass-per-charge, m/q, as $r_g = \frac{m}{q}\frac{v_\perp}{B}$) and record the positions of the beams on a microchannel plate (MCP) with sectored and radially separated anodes. FAST/TEAMS, Cluster/CODIF, and MAVEN/STATIC instead include time-of-flight (TOF) mass-separation systems that analyze the time taken for the ion to traverse a chamber of a known length, giving the velocity directly. The ion m/q can subsequently be found from the E/q, which is constrained by the ESA. Illustrations of the ion-optical assemblies of IMA and STATIC are shown in Fig. 3.

For each azimuthal sector and set energy, the ions are detected over a solid angle, $\Delta\Omega$, an effective aperture area, A^*, and an energy range ΔE, with an efficiency η. Together, these properties constitute the instrument's effective geometrical factor,

$$G_{\mathrm{E}} = \Delta\Omega A^* \eta \frac{\Delta E}{E} \ [\mathrm{cm^2\,s\,sr\,eV/eV}], \tag{7}$$

which is determined from calibration. The geometrical factor can be used to convert the detected ion counts into a physical value for the differential flux, j, by considering the count, c, of ions detected for the energy-directional bin over an integration time interval, Δt, so that

$$j = \frac{c}{G_{\mathrm{E}} \Delta t E} \ [\mathrm{cm^{-2}\,s^{-1}\,sr^{-1}\,eV^{-1}}]. \tag{8}$$

Each differential flux measurement effectively constitutes a sample of the local phase-space density distribution, f, as

$$j(\mathbf{r}, \Omega, E) = \frac{2E}{m_p^2} f(\mathbf{r}, \mathbf{v}), \tag{9}$$

where m_p is the particle mass of the measured ion species. However, this is a sample of the distribution that is detected in the reference frame of the spacecraft, which can be affected by the spacecraft potential and spacecraft ram velocity if the energy of the ambient (true) distribution in the inertial frame of the planetary body is comparable to the spacecraft potential, or the energy gained through the ram velocity. Analyses that account for spacecraft

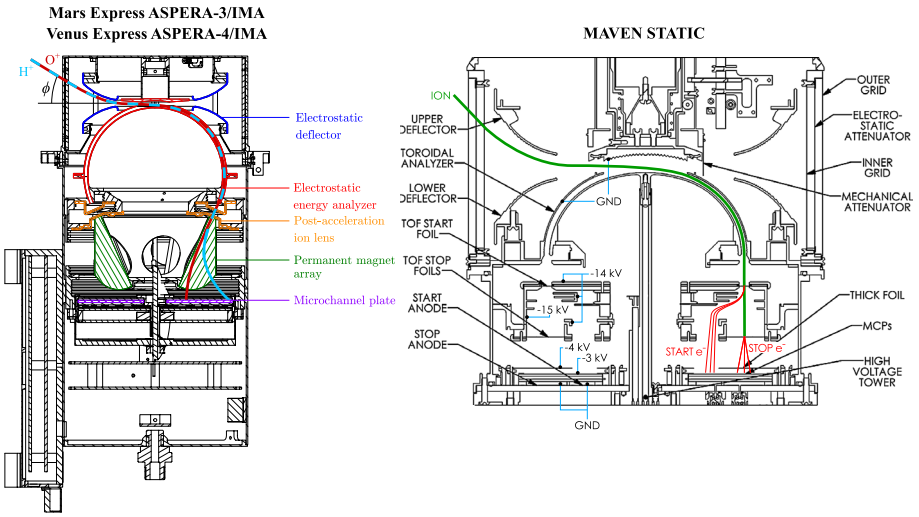

Fig. 3 Two examples of ion particle instruments used to measure ion escape, with traced particle paths in the hemicylindrical cut-away/cross-sections of the ion-optical assemblies. *Left*: The Ion Mass Analyzer (IMA) on Mars Express and Venus Express. A beam of H^+ (light blue) and O^+ (dark red) ions are drawn incident at an elevation angle ϕ and guided by a pair of electrostatic deflectors into a top-hat electrostatic energy analyzer (ESA). The ions with energies matching the energy setting of the ESA are post-accelerated by a 300–4200 V ion lens so that the nearly mono-energetic beam can be separated by gyroradii/mass-per-charge (m/q) in a permanent magnetic array. The O^+ strike the inner segments of a microchannel plate with sectored and radial anodes, while the H^+ ions strike the outer segments. Drawing of IMA adapted from Ramstad et al. (2017c). *Right*: The SupraThermal and Thermal Ion Composition Analyzer (STATIC) instrument on the MAVEN mission, which features a similar set of elevation deflectors and a top-hat ESA. Ions that pass the ESA (green curve) are post-accelerated by 15 keV before striking a thin-film carbon foil, generating a start pulse of secondary electrons (red curves) for a time-of-flight (TOF) velocity analyzer. After passing the 2 cm gap, the ions strike another carbon foil, generating stop pulse secondary electrons. Start and stop electrons are detected by a MCP with anodes segmented in azimuth and an inner (start) and an outer (stop) ring. The TOF between the start and stop signals determines the time in which the particle passed the cell, and thus the ion's velocity. The ion E/q is constrained by the ESA, from which the m/q of the ions can be separated. It should be noted that STATIC's ion optics (excluding deflectors) draw strongly on heritage from FAST/TEAMS and Cluster/CODIF. Drawing of STATIC adapted from McFadden et al. (2015)

potential and velocity have to consider Liouville's theorem, i.e. as the distribution is moved in velocity space the phase-space mass density is conserved, and correct the differential flux accordingly.

There are two commonly used methods of integrating the measured differential fluxes into a total escape rate. Each instantaneous measured distribution can be integrated moment-wise over space angle and energy (i.e. in velocity space) to find the macroscopic density (n), bulk velocity ($\mathbf{v}$), and temperature (T), from which the net flux can be calculated simply as $\mathbf{F} = n\mathbf{v}$. The calculated fluxes can be averaged by location in a suitable discretized coordinate system and integrated over an area that captures most, or ideally all, of the ion flux. While this is a computationally efficient method (once the moments are generated) some information is lost in the process as most space plasmas are not in thermal equilibrium. In addition the moments are only valid if the ion distribution is fully captured in the instrument's FOV and energy range, which is impossible to know a priori. In addition, a positive spacecraft potential can reflect low-energy ions before they enter the instrument, and a negative potential can shift the distribution to such high energies that the instrument cannot resolve it.

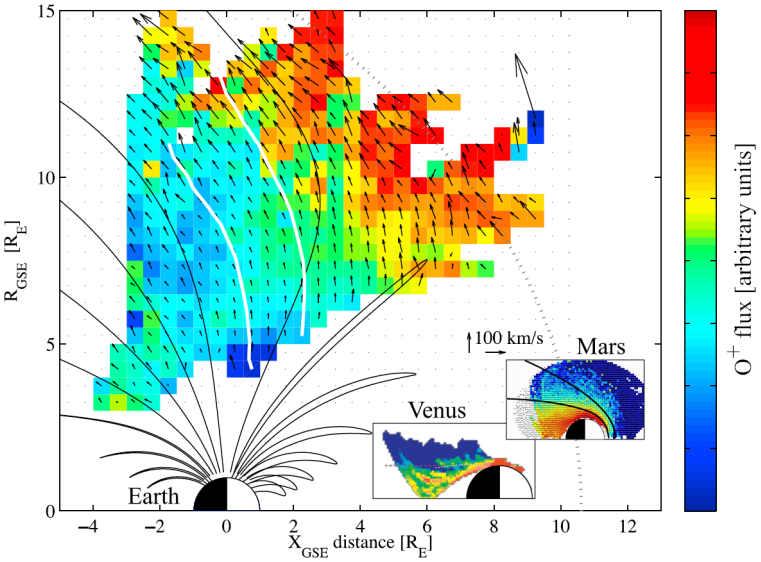

Fig. 4 Time-averaged O^+ outflows from Earth mapped in cylindrical coordinates, with analogous maps for Venus and Mars mapped inlaid on the same scale, contrasting the scale of the outflow and interaction area with the solar wind (Earth's magnetopause shown as dotted line) imposed by Earth's intrinsic magnetic dipole field, compared to the smaller induced magnetospheres of Venus and Mars. Red colors show high fluxes and blue colors show low fluxes in all maps, though the absolute values differ. Adapted from Nilsson et al. (2012a), Fedorov et al. (2008), and Ramstad (2017)

Alternatively, the measured distributions are sometimes averaged directly in a discretized phase-space coordinate system, the resulting average distribution function (ADF) can subsequently be integrated over velocity space to similarly yield moments of the ADF, or the average net flux directly. This method is computationally expensive, though has some advantages over the moments method. In particular; FOV or S/C-potential limitations of instantaneous measurements are less of a concern as long as the uncovered part of the velocity space is covered in later or earlier measurements of the same spatial location. In addition, the full ion distribution is preserved, thus the average energy of the outflow can be accurately derived. On the other hand, a disadvantage of averaging the measured distributions is that the average temperature cannot be derived, since natural variations in bulk velocities will alone broaden the average distribution, limiting the information available to interpret the physical mechanisms controlling escape.

Whether the measured distributions are averaged moment-wise or as an average distribution function, the escaping ion fluxes need to be integrated over a representative spatial area to obtain a global escape rate. The area varies significantly depending on the size of the obstacle, in particular the Earth's magnetic field creates a much expanded area of interaction with the solar wind and ion outflow, as shown in Fig. 4. However, choice of reference frame and coordinate system over which to map fluxes is not trivial and sometimes limited by the available instrumentation and/or orbit coverage. For example, at the Earth the atmospheric ions outflow to the magnetosphere and interplanetary space mainly from the polar cap and auroral oval (as illustrated in Fig. 2), which change area depending on the upstream solar wind and IMF conditions (Milan 2009). If the fluxes measured over the cap are averaged and multiplied by the area, rather than mapped out by complete coverage of the cap, then the change in area has to be considered if escape rates are calculated for different upstream

conditions. Similarly, calculations of escape rates in induced magnetospheres need to integrate fluxes both over the extent of scavenged ionospheric ions picked-up by the solar wind (Brain et al. 2015; Dong et al. 2017) and over the cross-section area of the induced magnetotail, which changes size depending on the upstream solar wind dynamic pressure and solar EUV (Edberg et al. 2009; Ramstad et al. 2017a).

Ion flows and the associated forces are organized by the magnetic field topology, which near the Earth, is in turn strongly dominated by the intrinsic magnetic dipole field and can be well-represented in the Geocentric Solar Magnetospheric (GSM) reference frame using Cartesian (e.g. Nilsson et al. (2012a)) or Magnetic Local Time/Invariant Latitude (MLT/ILAT) coordinates (e.g. Andersson et al. (2005)). In contrast, the structure and orientation of induced magnetospheres is mainly dependent on the upstream solar wind and IMF properties. The orientation of the induced magnetic field follows the upstream IMF clock angle $\phi_{\mathrm{IMF}} = \tan^{-1}(B_y/B_z)$, where B_y and B_z are Cartesian components of the upstream IMF defined in the Mars-Sun-Orbit (MSO) or Venus-Sun-Orbit (VSO) reference frames, depending on the planet in question. In MSO/VSO, X points towards the Sun, Z is oriented with the Martian heliocentric orbit normal, and Y completes the right-handed systems. The Mars-Sun-Electric field (MSE) or Venus-Sun-Electric field (VSE) reference frames are often used to represent the co-rotating fixed reference frame of the induced magnetospheres. In MSE/VSE, X is antiparallel to the upstream solar wind flow vector, Z represents the direction of the solar wind motional electric field ($\mathbf{E}_{\mathrm{mot}}$, see equation (2)), and Y again completes the right-handed systems (Dubinin et al. 1996). Mapping measurements in the MSE/VSE reference frames avoids mixing different outflow regions (and non-outflow regions). Regardless, with sufficient statistics, fluxes mapped in a cylindrical MSO/VSO reference frame result in the same escape rates, as found by Nordström et al. (2013) who calculated Venusian tailward ion escape rates by mapping the same set of VEX/ASPERA-4 measurements in cylindrical VSO and VSE coordinates separately. Highly directional radial escape channels (e.g. Mars' pick-up ion plume) may be more sensitive as the orbit coverage distribution could lead to potentially inhomogenous sampling of the bimodal distribution of IMF clock-angles. Note that planetary factors also influence the structure of the ion outflow in induced magnetospheres, in particular, dawn-dusk asymmetries due to the rotation of the upper atmosphere (Lundin et al. 2011), as well as Mars' crustal magnetic fields, which form mini-magnetospheres embedded in the ionosphere that can interfere with the $\mathbf{E}_{\mathrm{mot}}$-organization of the large-scale system (Nilsson et al. 2010; Fan et al. 2020).

3.2 Comparative Escape Rates

Over the last few decades, several studies have quantified global ion flow rates from in situ measurements, however, drawing conclusions from comparing studies can be difficult as the context of the measurements differ between studies, particularly the covered energy range in relation to the true distribution. Below, we briefly summarize the rates found by several key studies and some of the caveats involved in each. A comparison of escape rates and energy ranges for a selection of recent studies is shown in Fig. 5. A timeline of the measurements and reported escape rates, in relation to the solar cycle, is available in Fig. 6.

A number of terms are used in the literature to describe the relevant ion flow rates. There can be ion outflow from a planet, interchangeably referring to the rate at which ions flow away from the planet (but may later return as ion return-/inflows), or outflow may refer to the net outflow rate, which would be equivalent to the escape rate. This distinction is important as not all ions that outflow necessarily escape to space, rather, outflowing ions can be trapped on closed magnetic field lines or in the gravitational field of the planet and

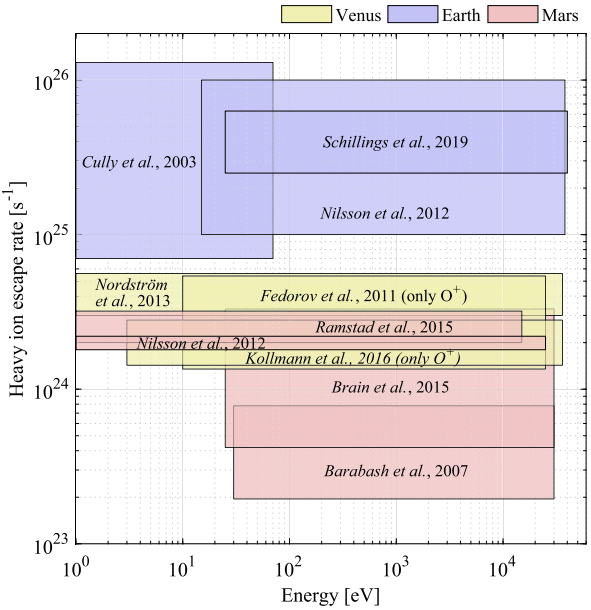

Fig. 5 Measured heavy ion (O^+ and heavier) escape rates from Venus (yellow colors), from Earth (blue colors), and from Mars (red colors) based on relatively recent studies under time-averaged/nominal upstream conditions of each planet, respectively. The horizontal limits of each box shows the specified energy range covered by the instrument in question. The vertical limits represent the uncertainties in the reported time-averaged escape rates or estimated ranges under nominal conditions, depending on the study. Note that these studies are based on measurements from varying altitudes and thus regions with corresponding variability in the characteristic ion energy. Additionally the studies represent varying phases of the solar cycle (see Fig. 6), the effects of cycle-driven upstream conditions are covered in Sect. 3.3

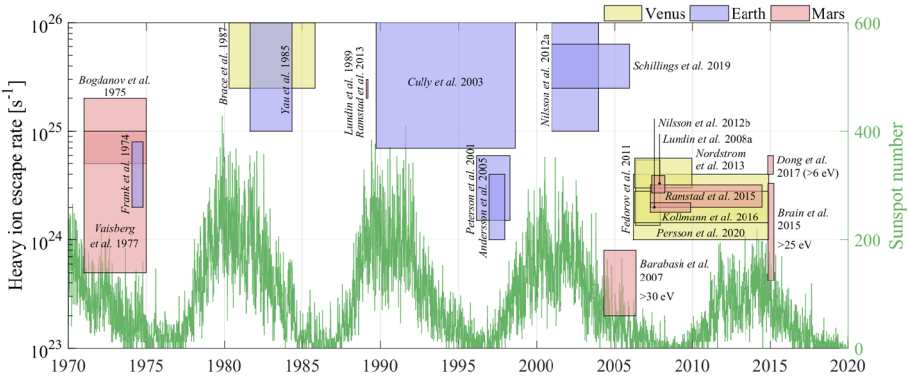

Fig. 6 Measured heavy ion (O^+ and heavier) escape rates from Venus, Earth, and Mars, over time and in relation to the solar cycle as indicated by the daily sunspot number (SILSO World Data Center 2020). The horizontal extent of each box indicates the time interval of measurements on which each study is based. The vertical extent represents either the reported uncertainty in the escape rate or, if a dependence was reported, the vertical extent represents the found escape rate under the respective nominal range of upstream conditions at each planet. In the studies that only report rates for a single heavy ion species, the complete heavy ion rate has been respectively estimated based on reported compositions at each planet for a more direct comparison

return for either reason. As such, while the ion escape rate can be calculated as the total net flow rate through any surface enclosing the region of ion production, the inflowing and outflowing populations can exhibit differing characteristic energies. Given that ion particle instruments typically have a lower energy limit well above thermal energies, it is not a trivial task to confidently find the escape rate by calculating the net cold ion flow rate. Ion upwelling is a closely related concept that generally describes density increases at unusually high altitudes (though still relatively low in that gravity is the dominating force), associated with relatively low-energy upward flows and/or an enhanced ambipolar electric field.

3.2.1 Earth

Particle instruments in the early era of near-Earth space plasma investigations were capable of observing ion distributions down to energies of a few 100's eV and without mass-resolving capability. At the time it was commonly assumed that the Earth's magnetosphere was populated by plasma almost entirely of solar wind origin as the ionosphere was considered shielded from the solar wind by the Earth's magnetic field. This picture changed with clear detections of keV O^+ ions during a geomagnetic storm from the "energetic-ion mass spectrometers" on the Advanced Space Technology Experiment (ASTEX) satellite (Shelley et al. 1972). The outflow was subsequently measured with increasingly improved sensitivity and detail by the International Monitoring Platform 7 (IMP-7) satellite, Explorer 31, Dynamics Explorer (DE-1/-2), Akebono, and Polar orbiters. An early estimated O^+ outflow rate of $\sim$0.1 kg/s ($\sim 4 \times 10^{24}$ s^{-1}) was reported by Frank et al. (1977) based on IMP-7 measurements of ions with energies 50 eV–45 keV.

Once measurements were available in lower energy ranges it became clear that the outflow rate was significantly higher. O^+ outflow rates between 10^{25}–10^{26} s^{-1} were later reported by Yau et al. (1985), based on measurements of 10 eV–17 keV ions from the Energetic Ion Composition Spectrometer (EICS) instrument on DE-1. Peterson et al. (2001) calculated substantially lower O^+ outflow rates of 3.0×10^{24} s^{-1} based on measurements in the 15 eV–33 keV range from the Toroidal Imaging Mass-Angle Spectrograph (TIMAS) on Polar. Similarly, Andersson et al. (2005) estimated an O^+ outflow rate of $\sim 2 \times 10^{24}$ s^{-1}, based on FAST/TEAMS measurements of 3 eV–10 keV O^+ distributions in 1997. Both the Polar and FAST measurements in these studies were taken during solar minima and thus indicated a strong solar cycle/seasonal dependence, which we elaborate on in Sect. 3.3.

The four formation-flying Cluster orbiters launched in 2001 and the mission is still operational at the time of writing, although the CODIF ion instruments are now significantly degraded. As such, most studies exclusively rely on data from the early phase of the mission. Nevertheless, Cluster provided ion measurements in a wide orbit ($\sim$16,000 km by $\sim$117,000 km perigee/apogee altitudes) that provides good coverage of energized ions escaping in the mantle and in the high-altitude cusp. Nilsson et al. (2012a) integrated Cluster/CODIF 40 eV–38 keV measurements from 2001-2003 in a cylindrical coordinate system and derived average O^+ escape rates "on the order of 10^{25} s^{-1}", i.e. consistent with the earlier measurements from DE-1 (Yau et al. 1985). More recently, Slapak et al. (2017) and Schillings (2019) (correcting Schillings et al. (2019)'s reported escape rates) have analyzed Cluster/CODIF measurements from 2001-2005 and find a wide range of O^+ escape rates depending on geomagnetic and upstream conditions, with values in the mid-10^{25} s^{-1} range under nominal conditions (shown in Fig. 5) and in the upper 10^{24} s^{-1} range under low EUV nominal solar wind conditions (i.e. solar minimum), consistent with the low altitude Polar and FAST measurements of escape fluxes during solar minimum (Peterson et al. 2001; Andersson et al. 2005).

3.2.2 Mars

Investigations of ion escape at Mars have yielded estimated rates in a perhaps more erratic evolution. The first direct measurements of atmospheric heavy ion fluxes were made by the 27 eV–20 keV Registrator Intensivnosti Electronov Protonov (RIEP) cylindrical ion spectrometers on the Soviet Mars 2, Mars 3 and Mars 5 missions in 1971 (Mars 2, 3) and 1974 (Mars 5). The first estimate of the Martian heavy ion escape rate was estimated based on 400 eV–4.0 keV RIEP measurements and reported by Bogdanov et al. (1975) as $\sim 10^{25}$ s^{-1}. Vaisberg et al. (1977) later took 10^{25} s^{-1} as an upper estimate and a review by Vaisberg and Smirnov (1986) gives a typical escape rate 10^{24} s^{-1}. Phobos-2, another Soviet orbiter, arrived at Mars in February 1989, close in time to the peak of the strong 22nd solar cycle. The onboard Automatic Space Plasma Experiment with a Rotating Analyzer (ASPERA) instrument comprised a top-hat electron spectrometer and an ion mass spectrometer, which performed nearly two months of measurements in Martian orbit, including four highly elliptic orbits from which Lundin et al. (1990) estimated an ion escape rate of 3×10^{25} s^{-1}.

The arrival of Mars Express in 2003 rapidly improved upon the limited statistics provided from the two month long Phobos-2 mission. Measurements from the ASPERA-3/IMA instrument were used by Barabash et al. (2007c) to derive an initial mission estimate of the total heavy ion (O^+, O_2^+, CO_2^+) escape rate of 4×10^{23} s^{-1}. This rate was surprisingly much lower than the previous estimates and it soon became clear that the 30 eV–36 keV measurements excluded a dominating low-energy population that persisted where MEX was measuring escaping ion fluxes. New energy tables were uploaded to the instrument, extending the lower end of the energy range to 10 eV in 2007 and again to $\sim$1 eV in 2009. The low-energy measurements were soon incorporated in analyses by Lundin et al. (2008b) and Nilsson et al. (2012b), reporting rates in the range 2.0×10^{24} s^{-1} to 3.3×10^{24} s^{-1} during solar minimum. Similar average rates of $(2.6 \pm 0.6) \times 10^{24}$ s^{-1} were later derived by Ramstad et al. (2015). The low-energy cold ion population was also excluded from the early MAVEN-derived heavy ion escape rate of $(0.4-3.3) \times 10^{24}$ s^{-1} (Brain et al. 2015), based on 25 eV–30 keV STATIC measurements. Later estimates of >6 eV fluxes by Dong et al. (2017) gave higher escape rates of $(2.0-3.0) \times 10^{24}$ s^{-1} for O^+ alone, indicating that a large fraction of the escaping ion distribution is low-energy in nature. Based on the O^+ escape rate reported by Dong et al. (2017), the equivalent total heavy ion escape rate would be roughly $\sim 6 \times 10^{24}$ s^{-1} assuming the ion flux composition reported by Carlsson et al. (2006).

3.2.3 Venus

Venus stands as the least explored planet of the trio, at least in terms of the surrounding plasma environment, yet a few studies have quantified the ion escape rate. Indirect estimates of the ion escape rate were provided by studies of the plasma properties of the nightside ionosphere using PVO magnetic field and Langmuir probe data, from which total plasma densities could be derived. With varying assumptions for the ion velocities, composition, and the size of the system, McComas et al. (1986) estimated an O^+ escape rate of $\sim 6 \times 10^{24}$ s^{-1}, while Brace et al. (1987) gave an order of magnitude higher rate of 5×10^{25} s^{-1}.

The arrival of Venus Express and the onboard ASPERA-4 suite in 2006 provided direct measurements of the ion distributions in the induced magnetotail, from which Barabash et al. (2007b) calculated an upper limit to the H^+ escape rate, and an H_2O stoichiometric 2:1 ratio of H^+:O^+ escape, from where an upper limit for the O^+ escape rate would follow as 5×10^{24} s^{-1}. VEX measurements collected during the following solar minimum were integrated to derive an O^+ escape rate "within a factor 2" of 2.7×10^{24} s^{-1} (Fedorov et al.

2011), similar to the recent estimate of (1–4) $\times 10^{24}$ s^{-1} by Persson et al. (2020). Considering Nordström et al. (2013)'s analysis of the VEX/ASPERA-4 data and the estimated total heavy ion escape rate $(4.3 \pm 1.3) \times 10^{24}$ s^{-1} (mapped in the VSE reference frame under steady IMF conditions), we can get a rough idea of the mass-composition of the escaping heavy ions as ∼50 % O^+ and ∼50 % heavier species, although the uncertainty is large. The energy table of ASPERA-4/IMA was 10 eV–36 keV from 2006–2010 and a new energy table was uploaded in 2010 that covered 2 eV–20 keV for the rest of the mission duration (2010-2014). However, setting a hard limit for VEX's sampling of the heavy ion distribution is not trivial as (1) the spacecraft potential was unquantified except for limited case-studies, and (2) VEX's orbit was extremely eccentric and thus reached high velocities near pericytherion, such that a stationary O^+ ion would be observed with a ram energy up to ∼8 eV in the spacecraft inertial reference frame, and analogously ∼16 eV for an O_2^+ ion.

3.3 Influence of Upstream Conditions

Without further consideration, it may appear as if the planetary ion escape rate is a fundamental constant in the solar system; wherever the heavy ion escape rate is measured, the rate is remarkably consistent, i.e. some factor times $10^{24}-10^{25}$ s^{-1}. This is despite large, sometimes several orders of magnitude, differences in atmospheric mass, planetary gravity, equilibrium temperature, upstream plasma and magnetic field conditions, solar EUV conditions, intrinsic magnetic field strength, etc. This also includes Titan (0.9×10^{24} s^{-1}; Coates et al. (2012)), and tentatively Pluto (0.5×10^{24} s^{-1}; McComas et al. (2016)), although these estimates are based on rare fly-bys, a single one in the case of Pluto.

However, we have known for a long time that the ion escape rate for any particular body is not constant, but rather a function of processes that drive the production and upward diffusion of ions, the rate of solar wind energy transfer, and the ion return/recycling efficiency. Such studies was pioneered by Yau et al. (1985), who found a strong dependence for the ion outflow from Earth on geomagnetic activity. Analogously, the ion escape rates measured, respectively, by Phobos-2 ($(2-3) \times 10^{25}$ s^{-1}); Lundin et al. (1985), Ramstad et al. (2013)) during the strong 1989 solar maximum (solar cycle 22), and Mars Express ($(2-3.3) \times 10^{24}$ s^{-1}; Lundin et al. (2008b), Nilsson et al. (2012b)) during the solar minimum between cycles 23 and 24, suggested that the heavy ion escape rate from Mars is highly dependent on the solar activity cycle.

Such dependencies are critical to quantify if we desire to understand the evolution of the planets in the solar system, and by extension, similar planets beyond. The primordial atmospheres of the terrestrial planets underwent intense impact erosion and hydrodynamic escape during the Sun's earliest phase (within ∼0.1 Ga of formation; e.g. Lammer (2013)) and the resulting secondary atmospheres have since evolved to their current state. The activity of the Sun, just like other stars, has evolved over time such that 4 Ga ago its EUV output was about an order of magnitude higher compared to the present (Ribas et al. 2005). For the period of time before ∼4 Ga, there is a large uncertainty in the early Sun's EUV output given the unknown initial rotational momentum of the Sun (Tu et al. 2015). The solar wind has undergone an even more dramatic evolution, as observations of Ly-α absorption in the astrospheres of analogous younger G-type stars suggest the solar wind flux was nearly two orders of magnitude stronger ∼4 Ga ago (Wood 2006). Naturally, we can no longer directly observe the planets' interactions with the young Sun, however, the variations in upstream parameters created by solar activity effectively provides conditions representative of the nominal conditions at different points in the time of the Sun's evolution. Extreme events, by present-day standards, created by solar flares and coronal mass ejections (CMEs), can

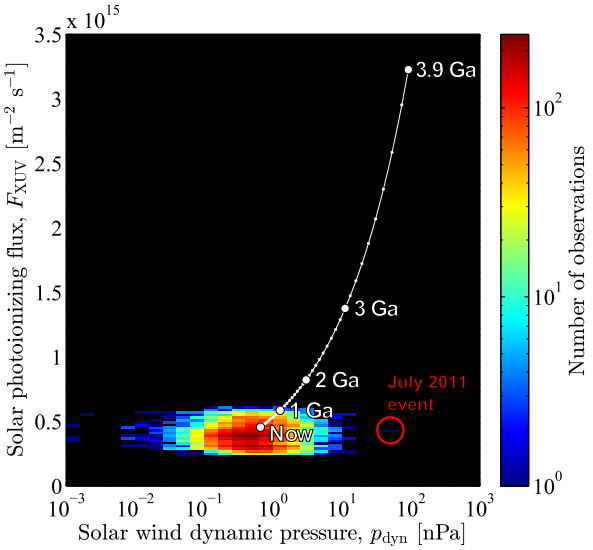

Fig. 7 Parameter space of upstream solar extreme ultraviolet (EUV) 1-118 nm ionizing photon flux and solar wind dynamic pressure at Mars sampled by the Mars Express orbiter over the course of a decade (2007–2017), compared with the evolution of the average parameters since 3.9 Ga ago. The limited time-equivalent coverage emphasizes the importance of determining ion escape dependencies over the available range, as well as the need to monitor and study extreme events. Adapted from Ramstad et al. (2018)

potentially supply upstream conditions partially representative of nominal conditions a few billion years ago, throughout the solar system. A major goal of planetary space weather studies is therefore to gauge the atmospheric escape responses to extreme events, such that the escape rate can be modeled as a function of the upstream conditions, and in turn, as a function of time.

Unfortunately, extreme events are by definition rare. For example, even after 14 years of operation, the parameter space of upstream conditions sampled by the Mars Express orbiter were in 2018 only representative of nominal conditions at most ∼1.1 Ga ago, as shown in Fig. 7. The rest of the range has to be covered by some method of extrapolation, which requires accurately quantified dependencies and some understanding of the state of the ion escape process. Some upstream parameters are also mutually correlated (such as solar wind density, IMF strength, and solar EUV irradiance), and potentially also correlated with seasonal changes in a planet's atmosphere, further complicating any analysis of upstream dependencies. Orbiting spacecraft have to be collecting statistics on ion fluxes for a long time, and over widely varying solar activity, such that escape rates can be calculated over a wide dynamic range for which any non-linear or co-dependent response can be accurately quantified, and that correlated parameters can be mutually constrained.

3.4 Influence of Solar Wind Conditions

3.4.1 Earth

A strong correlation between the O^+ outflow rate from the Earth's polar regions and geomagnetic activity (K_p, Dst) was established early on by Yau et al. (1985, 1988) based on low-altitude DE-1 measurements. Later studies using Akebono and Cluster data have found consistent trends and O^+ outflow and escape rates rising from the 10^{24} s^{-1} range under low-K_p conditions to the 10^{26} s^{-1} range under high K_p (Cully et al. 2003; Slapak et al. 2017). While the link to geomagnetic activity is only a 2nd-order dependence on the upstream conditions, this clearly shows that the escape of heavy ions depends on the amount of energy transferred to the magnetosphere-ionosphere system, as geomagnetic activity, through

coupling and total energy transfer, depends in turn on the upstream solar wind and IMF properties (Akasofu 1981; Vasyliunas et al. 1982).

If we want to understand how the Earth's magnetic field influences ion escape, then we need to compare Earth's dependencies with analogous trends for Venus and Mars. However, there is no strictly analogous, and directly comparable geomagnetic index for induced magnetospheres. Instead, we may more directly compare how ion escape depends on undisturbed upstream solar wind and IMF parameters at the planets. In this regard, Cully et al. (2003) also investigated the correlation of the O^+ outflow rate on a number of upstream factors and found the most consistent agreement with solar wind density, n_{sw}, solar wind velocity, v_{sw}, and cross-terms of both (e.g. flux, dynamic pressure, kinetic power flux). The main IMF-related influences were the solar wind motional electric field, E_{mot} (see equation (2)), and IMF variability. Using Polar/TIMAS measurements, Lennartsson and Collin (2004) instead binned the measurements in ranges of solar wind kinetic energy flux and Poynting flux, separately. They found strong dependencies on both, but also consistently higher rates for negative $B_{z,IMF}$, compared to positive $B_{z,IMF}$, indicating a strong IMF clock-angle dependence. Recently, Schillings et al. (2019) mapped escaping O^+ fluxes measured by Cluster in the mantle and high-altitude cusp versus upstream p_{dyn} for constrained high/low solar EUV intensities, and found a similar strong dependence on p_{dyn} for both of the EUV levels.

3.4.2 Mars

Such systematic studies of ion escape and the associated drivers were not feasible at Mars until the arrival of Mars Express in 2003, considering the limited datasets of measurements previously sampled by the Soviet Mars and Phobos-2 orbiters. Using the onboard ASPERA-3 suite of plasma particle instruments, the growing statistical base of ion flux measurements eventually allowed a number of studies to establish that the solar wind is a strong driver for the escape of ions with energies over 30 eV (Lundin et al. 2008a; Nilsson et al. 2010) and over 50 eV (Edberg et al. 2010; Wei et al. 2012). The lower boundary of 30 eV in these studies was imposed by the original energy table of the IMA instrument, covering a range of 30 eV–36 keV. New energy tables were uploaded to the spacecraft in 2007 and 2009, eventually extending the lower boundary to 1 eV. However, the ESA and deflector voltage tables required to reach these energies precluded use of elevation scanning at low energies, leaving IMA with a flat $360° \times 4°$ FOV for energies <50 eV, on a non-spinning spacecraft. This limited FOV precludes full coverage of the plasma distribution function for the instantaneous (192 s) samples of the distribution function, even during favorable pointing. As such, reliable moments cannot be directly calculated by integrating the measured distribution in the low-energy domain. To work around this problem, Nilsson et al. (2011) directly averaged the measured differential fluxes in a 4-dimensional cylindrically symmetric phase-space coordinate system. Over many orbits the sparse instantaneous samples below 50 eV collectively produced a fully sampled average phase-space distribution function. With the low-energy part of the distribution included, they found a much weaker increase in the heavy ion escape rate, a factor 1.6 when comparing high (80th percentile) solar wind flux conditions with average conditions.

The mentioned studies estimated the influence of the solar wind by comparing heavy ion measurements taken during varying upstream conditions. However, Lundin et al. (2008a) had already found that solar EUV (F10.7) is also a driver of ion escape at Mars, and extreme solar wind conditions are correlated with high EUV intensities due to a common dependence on the solar wind activity cycle. This correlation is particularly strong at Mars as both factors are also mutually modulated by the eccentricity of the Martian orbit, which varies

the heliocentric distance. By 2015 the available dataset of low-energy ion measurements had expanded greatly, and so had also the corresponding variations in upstream parameters, owing to the onset of solar cycle #24. To separate the effects of the solar wind and EUV as drivers for ion escape, Ramstad et al. (2015) divided the upstream SW–EUV parameter space in two EUV bins and combined the measured IMA heavy ion distributions in cylindrical phase-space ADFs, similar to the method developed by Nilsson et al. (2011), though the velocity space was kept 3-dimensional. The resulting heavy ion escape rates showed, in contrast to the previous studies, a potential weak inverse dependence on solar wind density, and no significant or consistent dependence on solar wind velocity, when EUV was constrained.

With the arrival of MAVEN at Mars in 2014 came the opportunity to get an independent view of the ion escape drivers, enhanced by the context provided by magnetic field vector measurements. The STATIC instrument on MAVEN has an energy range from 0.1 eV–30 keV with elevation sweeping throughout this range. Thus STATIC is capable of detecting the full range of cold heavy ions since even a stationary ion O^+ ion will gain a ram energy of 0.2–1.4 eV in the spacecraft inertial frame due to the orbital velocity. Dubinin et al. (2017) calculated the dependence of the average O^+ flux on several upstream parameters, and found a weak decrease in escaping O^+ flux with increased solar wind dynamic pressure. While a direct comparison cannot be made comparing average flux [cm^{-2} s^{-1}] and area-integrated escape rate [s^{-1}], Dubinin et al. (2017) noted that a decrease in the tail ion escape rate with solar wind dynamic pressure is consistent with the inverse n_{sw} dependence reported by Ramstad et al. (2015) based on MEX measurements. A weak inverse dependence on p_{dyn} was later also reported by Ramstad et al. (2018), based on MEX measurements.

Studies of the ion escape rate during space weather events offer a wider range of upstream conditions, although, individual events are not so straightforward to compare due to the rarity of strong events and the single-point nature of in situ measurements. MAVEN observed a CME impacting Mars in March 2015 during which the flux of high-energy pick-up ions on the dayside increased by over an order of magnitude (Jakosky et al. 2015). Such an increase in high-energy escaping fluxes is consistent with the statistical studies of >50 eV ions found by Edberg et al. (2010). In contrast, this may seem contradicted by the lack of an increase, and tentative decrease, in tailward 1 eV–15 keV escaping heavy ion fluxes during the strongest observed CME of solar cycle #24 as estimated by Ramstad et al. (2017c). The ions otherwise escape as a relatively cold (below few 10s eV) outflow, likely these are accelerated to higher energies and increasingly escape on the dayside as scavenged ions during strong space weather events, resulting in a largely unaffected global ion escape rate.

3.4.3 Venus

Few have systematically studied the influence of upstream solar wind parameters on ion escape at Venus. Given that Venus features a Mars-like induced magnetosphere, one might expect that ion escape rates should depend similarly on upstream parameters, at least to the first order. Similar to their study at Mars (Edberg et al. 2010), Edberg et al. (2011) integrated Venus Express ASPERA-4/IMA measurements separately for storm times (CME and CIR impacts) and quiet times. Comparing the two, they found that Venusian O^+ escape rates increased by roughly a factor $\times 2$ during storms. Although they did not methodically constrain EUV levels, the measurements were acquired during 2006–2010 when EUV levels were consistently low. Recently, Masunaga et al. (2019) have analyzed the full VEX/IMA dataset and derived escape rates from ion moments, separating the measurements in bins of upstream p_{dyn}, E_{mot}, and EUV. The latter constrained by separating measurements taken before/after Dec. 31 2010, corresponding to a rapid increase in the F10.7 index at the onset

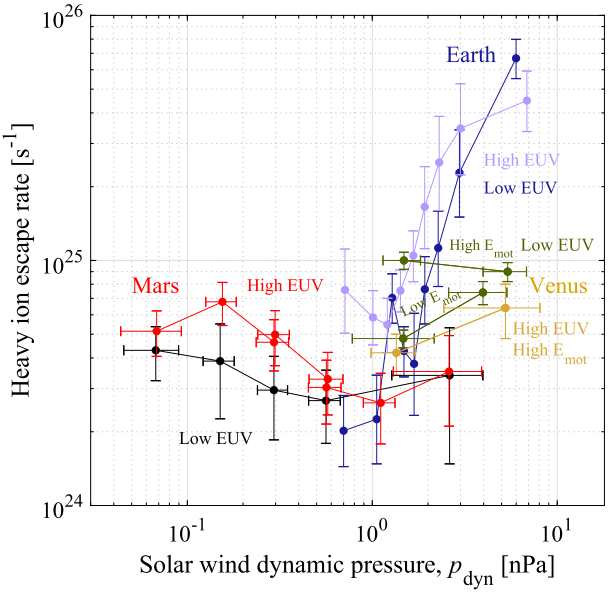

Fig. 8 Escape rates of heavy ions ($M/q \geqslant 16$) from Venus (Masunaga et al. 2019), Earth (Schillings 2019), and Mars (Ramstad et al. 2018); as dependent on upstream solar wind dynamic pressure for individually constrained ranges of solar EUV. At Venus, Masunaga et al. (2019) divide the VEX dataset in time as before/after 31 Dec. 2010, corresponding to the transition from solar minimum to maximum and an abrupt increase in the F10.7 index, a solar EUV proxy. At Earth, Schillings (2019) divides the Cluster dataset by below/above a solar 0−90 nm EUV intensity of 3.5 mW/m^2. At Mars, Ramstad et al. (2018) map escape rates over a 2D upstream parameter space, here we show the estimated escape rates from Mars for solar 0−118 nm photon flux above 4.7×10^{14} m^{-2} s^{-1} (red) and below 3.5×10^{14} m^{-2} s^{-1} (black), separately

of solar cycle #24. Their results show a moderate relative increase (∼50 %) in O^+ escape rates with increased p_{dyn}, for similar EUV levels. In addition, Persson et al. (2020) also recently found a stronger increase in the O^+ escape rate (roughly 5×) across the range of solar wind energy fluxes observed by VEX, indicating that upstream solar wind energy flux may be a more direct driver for ion escape at Venus.

3.4.4 Comparative Rates and Trends

Each planet is at a different average distance from the Sun, from which it follows naturally that the typical solar wind conditions will also differ since the solar wind density decreases with distance from the Sun roughly as r^{-2}. However, the variations in solar wind parameters at each planet provides some overlap in the distributions, for which the planets are subjected to similar upstream solar wind. Figure 8 shows the how the rate of heavy ion escape depends on upstream solar wind dynamic pressure, and how the rate of escape compares between the planets for similar p_{dyn} under constrained solar EUV. The trends here are taken from recent studies based on measurements from Venus Express (Masunaga et al. 2019), Cluster (Schillings 2019), and Mars Express (Ramstad et al. 2018). The values for the upstream p_{dyn} used in Masunaga et al. (2019) were personally provided by Kei Masunaga and included in Fig. 8. In addition, the escape rates shown for Venus have been multiplied by a factor 2 to account for the exclusion of O_2^+ escape in the study. With the escape rates plotted on the

same scale, we may immediately deduce that Venus, Earth, and Mars all feature similar ion escape rates in the few 10^{24} s^{-1} range around 1–2 nPa.

The dependencies on p_{dyn} are highly divergent between the planets. Respectively, Fig. 8 shows that:

- The Venusian ion escape rate increases weakly with p_{dyn}.
- The Martian ion escape rate decreases weakly with, or is insensitive to p_{dyn}.
- The Earth ion escape rate increases dramatically with p_{dyn}, rising by nearly two orders of magnitude over one order in p_{dyn}.

As such, it is quite clear, not only that the average atmospheric ion escape rate from Earth is higher than the rates from Mars and Venus on average, but also the escape rate from Earth is significantly more sensitive to the kinetic energy of the solar wind.

3.5 Influence of Solar Extreme Ultraviolet (EUV) Radiation

From Fig. 8 we may also deduce that increased EUV does not have the same effect on all three planets. Overall the heavy ion escape rate appears to increase with EUV at Mars (Dong et al. 2017; Ramstad et al. 2018) and at Earth (Schillings 2019), while the escape rate from Venus is lower at high EUV as measured with VEX (Masunaga et al. 2019).

3.5.1 Earth

Early studies of ion outflow from Earth found a positive correlation with the F10.7 EUV proxy (Cully et al. 2003; Yau et al. 1988), though without constraints on correlated upstream solar wind parameters. Recently Schillings et al. (2019) also calculated the O^+ escape rate for separate bins of 0-90 nm EUV irradiances based on Cluster measurements in the mantle and high-altitude polar cap, effectively constraining the solar wind dependence within each bin, and found no dependence. This was shortly thereafter shown to be an instrumental artifact and is corrected by Schillings (2019), yielding an increase with EUV for O^+ fluxes in both regions, consistent with the previous studies and also deconvoluting the solar wind dependence from the correlated EUV dependence. While an increase in outflow observed at low altitudes could return in a different location or at an energy outside the respective instrument's energy range, the mantle ions are nearly all expected to escape.

Others have studied ion escape and its dependence on EUV at high altitudes using Cluster's Electric Field and Waves (EFW) instrument (André 2015; Li et al. 2017), showing that increased EUV increases the flux of a low-energy ion population that is undetectable by the CODIF instrument. However, this method is unable to distinguish between H^+ and O^+ ions and the low energy-population is expected to be dominated by H^+ ions (André 2015).

3.5.2 Mars

Nearly all studies of ion escape drivers at Mars find a consistent increase in the heavy ion escape from the planet with higher solar EUV levels. Mars Express was the first mission carrying an ion instrument to also operate long enough to enable studies of solar EUV as an ion escape driver. IMA measurements over the course of the decaying 23rd solar cycle led Lundin et al. (2008a) to find a steady increase in the escape rate with the F10.7 index. While Phobos-2 did not operate long enough to collect the statistics necessary to separate

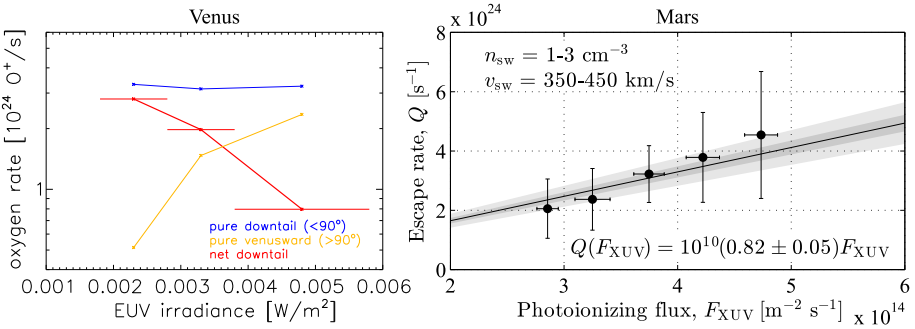

Fig. 9 Heavy ion escape rates of Mars and Venus for various levels of upstream solar EUV. Left: O^+ flow rates from Venus, adapted from Kollmann et al. (2016). The net escape rate (red curve) decreases with increasing EUV due to an increase in the return (venusward) flow rates (yellow curve) acting on a constant outflow rate (blue curve). Right: Heavy ion (O^+, O_2^+, CO_2^+) tailward escape rates from Mars for bins of upstream 1-118 nm solar ionizing photon flux and constrained nominal solar wind properties, adapted from Ramstad et al. (2017b). The line shows a fitted linear function constrained at the origin, as such, heavy ion escape from Mars follows a near-linear dependence on photoionizing X-ray and EUV flux

upstream drivers, Lundin et al. (2013) later put the Phobos-2 measurements from Ramstad et al. (2013) in context with the Mars Express measurements on an F10.7 scale, showing that the Phobos-2 measurements in context also indicate a dependence on EUV.

Utilizing the growing statistical database of ion flux measurements and the onset of solar cycle #24, Ramstad et al. (2015) separated IMA measurements in the tail by upstream conditions in bins of solar wind density, velocity, and high/low 10-124 nm EUV intensity, effectively constraining any possible influence of solar wind correlated with the two EUV levels. The heavy ion escape rates were consistently higher for stronger EUV intensities compared to the bins of weaker EUV. Subsequently, Ramstad et al. (2017b) reported that the ion escape rate dependence on EUV was more consistent for EUV photon flux, rather than EUV irradiance (energy flux). They separated the IMA measurements in several bins of X-ray/EUV 1–118 nm photon flux, while constraining the solar wind to nominal conditions, resulting in a clear linear dependence for the downtail heavy ion escape rate (see Fig. 9), in particular the increase in the tail fluxes was shown to be composed of cold (<50 eV) ions. A similar trend was also reported by Dubinin et al. (2017) as an increase in low-energy (<30 eV) tailward cold ion flux with EUV. Similarly, Dong et al. (2017) used MAVEN/STATIC data to infer a similar increase in the downtail escape of O^+, while also reporting the strongest increase among the low-energy ions. Dong et al. (2017) also constrained the upstream IMF strength using MAVEN's magnetometer measurements, in addition to the solar wind dynamic pressure. The magnetic field measurements also allowed them to study EUV influence in the MSE reference frame for the first time, and separate the escape rate through the "plume" channel of scavenged ionospheric ions picked-up by the solar wind. Interestingly, these pick-up ions showed no significant increase with EUV, in contrast with the tailward escape. Most recently Ramstad et al. (2018) calculated escape rates using MEX measurements over a binned 2D p_{dyn} and 1-118 nm photon flux upstream parameter space and modeled the dependence using a 2D power function. The modeled function also showed a linear dependence on the 1–118 nm flux, however the characteristic energy of the already low-energy cold ions decreases further as solar EUV increases.

3.5.3 Venus

Systematic studies of solar EUV influence on ion escape from Venus were absent until Kollmann et al. (2016) divided up the VEX ASPERA-4/IMA dataset into three bins of upstream 0-90 nm solar EUV intensities and calculated the average O^+ distribution function for each bin. In clear contrast to the EUV trend at Mars, they found that increased EUV decreases the O^+ escape rate from Venus. The decreasing trend is a result of Venusward (return) flows in the induced magnetotail that increase with EUV, decreasing the net escape rate. The tailward, return/venusward, and net flow rates from Kollmann et al. (2016) are shown in Fig. 9. Recently, a potential decrease in the O^+ escape rate between solar minimum and solar maximum has also been reported by Persson et al. (2018), using a similar method to integrate O^+ fluxes measured by Venus Express, although the decrease is on a similar scale as the uncertainties in the derived escape rates. The change in escape rate with EUV in these studies could hypothetically be conflated with the associated change in solar wind properties, however, Masunaga et al. (2019) recently calculated the escape rates using integrated VEX/IMA moments, binned by time (EUV), upstream solar wind dynamic pressure, and $|E_{\mathrm{mot}}|$. Similar to Kollmann et al. (2016), their results show an overall decrease in the escape rate with EUV, though also a strong variability between the low EUV bins as shown in Fig. 8.

4 A Generalized Understanding of Ion Escape

To the first order, we might expect that any two similar planets would also exhibit similar escape characteristics, reflecting their shared planetary properties. However, comparing Mars and Venus, i.e. two non-magnetized planets, we find opposite dependencies on solar EUV and a positive solar wind dependence on solar wind dynamic pressure only for Venus. Similarly, comparing Venus and Earth, two planets of comparable size and gravity, the O^+ escape rate from Venus decreases with solar EUV, while O^+ escape from Earth increases with EUV. Ion escape from Earth is also strongly dependent on the dynamic pressure of the solar wind, which only weakly affects escape from Venus. To explain the differences in the ion escape trends we need to consider the differences in the planetary properties as carefully as their similarities, which may affect the energy required for escape, the ion supply rate, or the location of ion production and thus also the escape efficiency.

4.1 Energy- and Supply-Limited Escape

Fundamentally, ion escape involves a series of connected processes. In order for an ion to escape it has to be produced by ionization of a neutral particle, which in the inner solar system, sees the ion production rate dominated by photoionization from solar EUV absorption, with generally small contributions also from charge-exchange and electron impact ionization. Most of these ions will be produced in the dayside lower ionospheres of Venus, Earth and Mars, i.e. below the exobase. In order to energize these ions without collisionally spreading the energy to the much more numerous ambient neutrals, i.e. for effective non-thermal escape, the ions have to diffuse upwards above the exobase before re-neutralizing e.g. by charge-exchange or recombination with a free electron. In addition, the energy transferred from the solar wind is not necessarily strongest near the exobase, but typically rather in regions at significantly higher altitudes. We may consider that there is a total ion supply/source rate, Q_S, that can be defined as the rate of gravitationally bound ions entering this energization region. The upward rate of diffusion depends on the ion density on the lower side, the

temperature, T, of the thermosphere, but also on the horizontal magnetic field component, B_h. In the Bohm diffusion regime;

$$Q_S \propto Q_{P,low} T / B_h + Q_{P,high}, \tag{10}$$

where $Q_{P,low}$ is the production rate of the ion species in question in the diffusive lower ionosphere. In addition, some neutral species have larger scale heights than others and may in a relatively small, though significant, part to be produced directly inside the energization region at a rate $Q_{P,high}$, effectively bypassing the diffusion process.

Next, we ought to consider how many ions can be driven to escape using the energy delivered to the energization region. This equivalent rate can be taken as

$$Q_E = f_{\text{esc}} k_c \frac{P_{\text{sw}}}{E_{\text{esc}}}, \tag{11}$$

where P_{sw} is the available solar wind power integrated over the interaction area, k_c is the coupling coefficient with the energization region, f_{esc} is the fraction of power transferred to the supplied ions available for escape, and E_{esc} is the escape energy of the ion species being considered at the altitude of the volume. As such, the unit of Q_E is [s^{-1}].

We should also consider the efficiency of the escape process. Ions that are energized to energies over E_{esc} waste energy. In addition, ions that are energized but sent on trajectories that precipitate back into the atmosphere waste both supplied ions and energy, leading to an inefficient escape process. For example, magnetized ions on closed magnetic field lines may not escape unless these become sufficiently energized to demagnetize, or be ejected in bulk as plasmoids. Similarly, even ions on open field-lines but produced at low altitudes may have a particularly narrow loss domain in phase-space, leading to low efficiencies. In contrast, at Mars and Venus the outer coronae are immersed in the solar wind flow, ions produced here (by photoionization or charge-exchange with solar wind protons) will be picked up by the $-\mathbf{v} \times \mathbf{B}$ motional electric field of the solar wind. This escape process is both energetic and effective, yielding ions with energies on the order of 10's keV and mostly open efficient paths to escape. Estimating the escape efficiency is a complex matter that will depend on the origin of photoion production and the type of energization (heating or acceleration), as well as the size of the system and its magnetic field topology, which, in turn, depend on the prevailing upstream solar wind, EUV, and IMF conditions. In practice, however, the rate of precipitating energized ions, relative escaping ions, can be measured directly.

We do not attempt to model these bottlenecks here, but rather consider how the relative size of these quantities may limit the rate of ion escape and the efficacy of the upstream drivers. The limiting factor effectively determines the state of the system as supply-limited or energy-limited, with the escape rate additionally limited by the ion transport efficiency. We should consider how the upstream drivers, such as solar wind, solar EUV, and IMF, may affect the supply, energization and efficiency of ion escape as illustrated in Fig. 10. By comparing with the observed escape response (see Figs. 8 and 9) we can infer the state of ion escape for each planet. For example, solar EUV will both produce more ions, increase the temperature of the thermosphere and drive increased upwelling of ions by creating energetic photoelectrons that set up an ambipolar electric field, all these factors increase Q_S.

Stronger solar wind provides more energy for the system, increasing the number rate of ions that can be energized to escape energy (Q_E), however, in the process the downward Poynting flux into the system may also drive Joule heating in the upper atmosphere, increasing the temperature and thus the ion diffusion rate. On the other hand, in the case of non-magnetized planets, the increase in magnetic pressure required to balance the dynamic

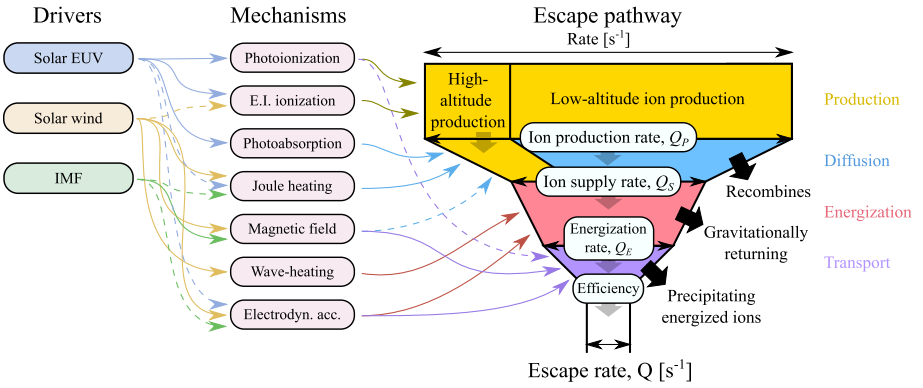

Fig. 10 Drivers, mechanisms, and pathway of ion escape conceptualized for an energy-limited system. Each subsequent step is a potential bottleneck that may define the limitation state of the system, for example here, increasing Q_S will not increase Q as Q_E is the smaller of the two. Solar wind and solar EUV act as drivers that regulate mechanisms, which in turn alters the rate of ion supply and energy transfer. Solid arrows indicate causal links, dashed arrows indicate possible but undetermined links

pressure of the solar wind can magnetize the ionosphere if the magnetic pressure exceeds the ionosphere thermal pressure (e.g. at Mars (Dubinin et al. 2008)), and may thus decrease Q_S as follows from equation (10). Another potential factor that has barely been explored in empirical studies is the influence of the upstream IMF, which determines the strength of the solar wind motional electric field through equation (2). As we will explore next, the strength of the electric field in the magnetosheath influences the quasi-steady (DC) component of the dynamo power induced by the interaction, and thus the coupling between the solar wind and the magnetosphere-ionosphere system.

4.2 Solar Wind Coupling and Energization

The electromagnetic forces that accelerate or heat atmospheric ions are mainly powered by the electrodynamic interaction with the solar wind. In addition to its kinetic energy, the undisturbed solar wind also carries Poynting flux,

$$\mathbf{S} = \mathbf{E} \times \mathbf{B}/\mu_0, \tag{12}$$

unless its flow is parallel to the IMF, whereby $|\mathbf{E}_{\text{mot}}| = 0$. However, the bulk of the electrodynamic power in magnetospheres is generated by induced currents at the bow shocks and at the magnetopauses/IMBs. Electrodynamic power,

$$P = \mathbf{E} \cdot \mathbf{J}, \tag{13}$$

is generated where the induced current flows against the local electric field, such that the local value for P is negative, i.e. power is drawn from the kinetic energy of the plasma and transferred to the local electromagnetic field. In intrinsic magnetospheres, the magnetopause Chapman-Ferraro current system (Chapman and Ferraro 1931) is controlled by the direction of the intrinsic magnetic field, presenting a complicated picture where the sign of P in any region of the magnetopause is dependent on the direction of the IMF clock-angle, which in-turn controls the direction of $\mathbf{E}_{\text{mot}}$ in the magnetosheath, illustrated in Fig. 11.

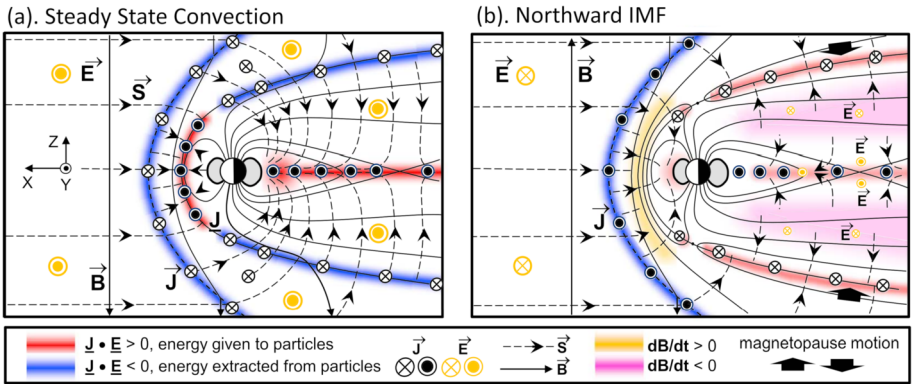

Fig. 11 Electrodynamic power generator regions (blue colors), load power regions (red colors), and Poynting flux (dashed lines) in Earth's magnetosphere. **a**) Under southward IMF conditions. **b**) Recovery under northward IMF conditions. The directions of the magnetopause currents in intrinsic magnetospheres are controlled by the orientation of the intrinsic magnetic field, thus the direction of the electric field determines whether the magnetopause acts as a dynamo or load region. Adapted from Lockwood (2019)

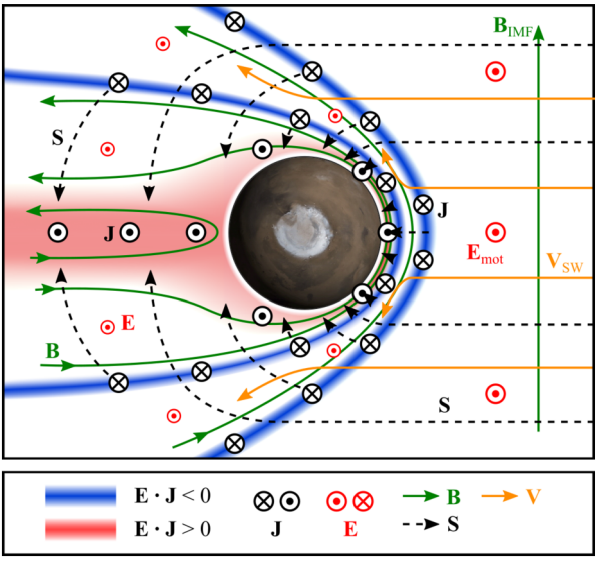

Fig. 12 Illustration of solar wind energy transfer in an induced magnetosphere under ideal perpendicular IMF conditions. The pile up of the IMF induces currents, **J**, at the bow shock and IMB that flow in a direction opposite to the solar wind motional electric field, $\mathbf{E}_{mot}$ so that $\mathbf{E} \cdot \mathbf{J} < 0$, thus the bow shock and IMB act as dynamo regions (shaded blue), generating electromagnetic power that transfers into the magnetosphere as Poynting flux, **S**, and powers load regions $\mathbf{E} \cdot \mathbf{J} > 0$ in the conductive ionosphere and the gyroconductive induced magnetotail. Based on Saunders and Russell (1986) and Ramstad et al. (2020)

In contrast, induced magnetospheres freely reorient their current systems with the orientation of the draped IMF so that the magnetosheath currents always flow in the electric southward direction (Ramstad et al. 2020), as such, both the IMB and BS currents in induced magnetospheres always act as dynamo/generator regions. The southward flow of charge against the solar wind electric field subsequently powers a magnetospheric convective electric field that drives currents in the conductive ionosphere and gyroconductive induced magnetotail (Lyons and Speiser 1985). In Fig. 12 we can see that power is transferred from the dayside and flanks of the induced magnetosphere where the Poynting vector is directed inwards. In this region the solar wind flow is nearly field-aligned with the draped IMF, therefore the inward Poynting flux is small.

The power transfer from the solar wind to intrinsic magnetospheres can be estimated through e.g. the Vasyliunas coupling function (Vasyliunas et al. 1982), which we here formulate as a simplified expression:

$$P_{\text{in}} = \rho_{\text{sw}} v_{\text{sw}}^3 A_{\text{eff}}(p_{\text{dyn}}, M_A) k(M_A, \theta_{\text{CA}}). \tag{14}$$

Besides the previously defined parameters, here A_{eff} is the effective magnetosphere-solar wind interaction area, k is a dimensionless coupling coefficient, M_A is the magnetic moment of the planet, and θ_{CA} is the IMF clock-angle relative the dipole orientation of the planet. The interaction area is at least as large as the cross-section area enclosed by the magnetopause, the distance of which we approximate as the balance point of magnetic pressure and solar wind dynamic pressure $R_{\text{MP}}^6 = \mu_0 M_A^2 / 64\pi\rho_{\text{sw}} v_{\text{sw}}^2$. Thus, $P_{sw} = 0.5\rho_{\text{sw}} v_{\text{sw}}^3 A_{\text{eff}}$ is the total amount of solar wind kinetic energy flux that intersects the magnetosphere. The coupling coefficient, k, is parameterized by the scaling factor a, yielding the derived expression

$$P_{\text{in}} = B_T^{2a} \rho_{\text{sw}}^{2/3-a} v_{\text{sw}}^{7/3-2a} G(\theta_{\text{CA}}) M_A^{2/3} \mu_0^{1/3-a}, \tag{15}$$

where B_T is the IMF strength in the plane perpendicular to $\mathbf{v}_{\text{sw}}$, and $G(\theta_{\text{CA}})$ is the coupling dependence on the IMF clock angle. Various studies have estimated the dependence on a, with recent results ranging at least from $a = 0.3$ (Finch and Lockwood 2007) to $a = 0.5$ (Tenfjord and Østgaard 2013). Schillings et al. (2019) found the strongest correlation of O^+ escape with the estimated value $a = 4.3$ and $G(\theta_{\text{CA}}) = \sin(\theta_{\text{CA}}/2)^{2.7} + 0.25$ from Wang et al. (2014).

Estimates of solar wind coupling with induced magnetospheres lack such an analytical model, at least to our knowledge. However, the ion escape coupling efficiency was empirically estimated by Ramstad et al. (2017b) through comparing the solar wind interaction area and the total energy of tailward escaping ions. For comparison, we can obtain corresponding values for Earth's magnetosphere by taking upstream values from the OMNI database and plugging them into equation (15). The resulting estimated values are shown in Fig. 13, along with a comparison to the directly measured values for Mars. We may note that the average coupling efficiency is lower than for Mars, however, coupling efficiency with the Earth is constant for the middle and upper part of the range, while coupling with Mars decreases with increasing solar wind p_{dyn}. For both planets, the total amount of energy transferred to the system still increases with increasing dynamic pressure, though the decreasing coupling efficiency with Mars implies that it is less sensitive to variations in solar wind p_{dyn}.

Alone, this quasi-static (DC) model of electrodynamic interaction in induced magnetospheres implies that the coupling during parallel IMF (small angle between $\mathbf{v}_{\text{sw}}$ and $\mathbf{B}_{\text{IMF}}$) should approach zero since $\mathbf{E}_{\text{mot}}$ becomes negligible. In such cases, the Faraday and AC induction terms instead dominate the electrodynamic nature of the interaction as evident from the current systems inferred by Dubinin et al. (2013), and the lower, though still significant, Venusian ion escape rates under relatively low $\mathbf{E}_{\text{mot}}$ upstream conditions found by Masunaga et al. (2019).

As we investigated earlier in this chapter, solar EUV can also affect the ion escape rate, which may relate to the influence of EUV on solar wind coupling. Increased ionizing radiation will increase the production rate of ions and electrons, and by extension the plasma density, in effect altering the coupling by increasing the conductivity of the upper atmosphere, which regulates e.g. load currents and ohmic dissipation, magnetic diffusion rates, and the magnetospheric convective electric field. At unmagnetized planets, the induced magnetospheres are formed entirely by the magnetic pressure gradient resulting from the induced currents, thus we may expect solar EUV to play a large role in influencing coupling also

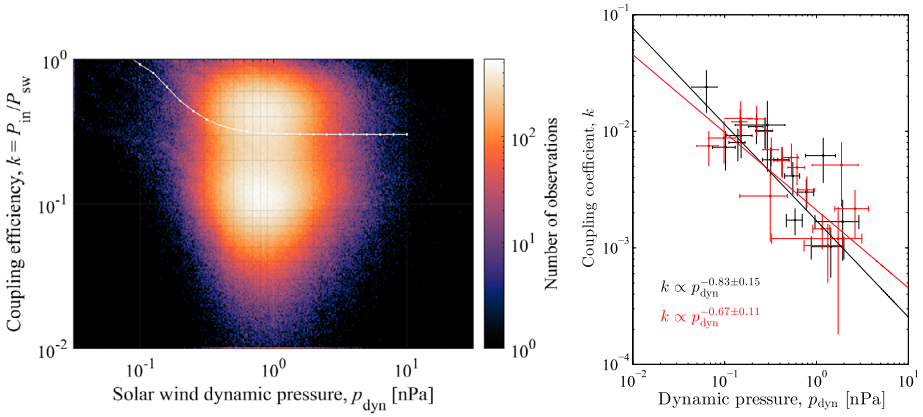

Fig. 13 Left panel: Solar wind coupling efficiency with Earth's intrinsic magnetosphere shown as a distribution plotted against upstream solar wind dynamic pressure. The coupling efficiency is calculated as the fraction of power entering the induced magnetosphere based on the formula from Vasyliunas et al. (1982) shown in equation (15), over the total amount of solar wind kinetic power intersecting the magnetosphere, i.e. $P_{sw} = \rho_{sw} v_{sw}^3 A_{eff}/2$. The white curve shows the average value of k for corresponding bins of p_{dyn}. Right panel: Solar wind coupling efficiency with Mars induced magnetosphere as a function of upstream solar wind dynamic pressure under low solar EUV (black colors) and high solar EUV (red colors), adapted from Ramstad et al. (2017b). Total transferred power depends on A_{eff}, which is much larger for Earth

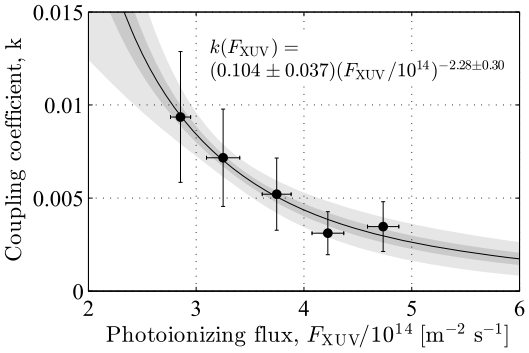

Fig. 14 Coupling efficiency between escaping heavy ions in the Martian induced magnetosphere and the upstream solar wind as a function of 1-118 nm X-rays and Ultraviolet (XUV) ionizing photon flux, for constrained upstream solar wind conditions. Adapted from Ramstad et al. (2017b)

in such systems. A systematic study of the influence of EUV on ion escape from Mars was included in the study by Ramstad et al. (2017b). Shown in Fig. 14, increased EUV flux decreases the coupling of the solar wind with escaping ions inside the induced magnetosphere. While Mars features crustal magnetism, and the crustal fields' influence on the global system is not well understood, Mars' interaction with the solar wind is dominated by the induced component. Nevertheless, the solar wind interaction with Mars is at least in part a hybrid system (intrinsic and induced; as inferred e.g. by DiBraccio et al. (2018)), which could make a significant difference compared to truly pure induced systems, such as the Venusian induced magnetosphere.

At the Earth, higher solar EUV flux conversely appears to increase the coupling with the solar wind by increasing the conductivity of the polar ionosphere, resulting in stronger field-aligned Birkeland currents and the associated Poynting flux to enter the cusp and ionosphere (Ohtani et al. 2014). The fraction of this increased precipitating Poynting flux that energizes ions, rather than Joule-heats the neutral polar atmosphere, remains to be deter-

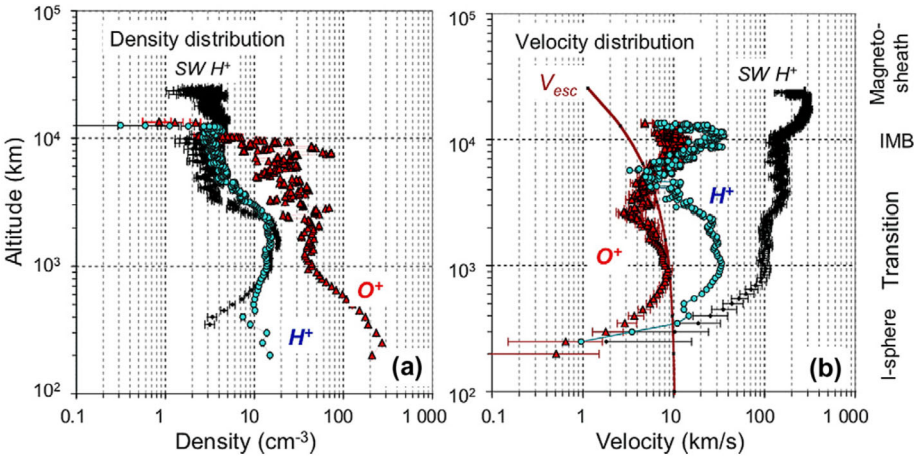

Fig. 15 Ion densities and velocities in the noon-midnight plane at Venus. The O^+ distribution in the induced magnetotail is gravitationally bound up to high altitudes as indicated by the escape velocity, v_{esc}. Adapted from Lundin et al. (2011)

mined and the purely solar wind-ion escape coupling could have a different dependence on EUV.

4.3 Bound and Escaping Populations, Return Flows

Despite the decreased energy transfer rate with EUV/XUV shown in Fig. 14, the ion escape rate from Mars still increases with EUV, as we showed in Fig. 9. Observationally, the decrease in coupling mainly occurs due to a decrease in accelerated ions (>50 eV), while the increase in escape rate is due to a larger increase in cold ion outflow. However, the characteristic energy of cold ion escape drops with increased EUV (Ramstad et al. 2018), thus if EUV increases further, the cold ions could reach a point where the energy of the outflow is less than the escape energy, which would result in gravitationally returning flows. The lack of gravitationally bound return flows at Mars indicates that the outflowing ions have sufficient energy to escape under the full range of observed upstream EUV conditions. It is possible that this could change under even higher solar EUV fluxes, however, lacking measured spacecraft potentials for Mars Express, Ramstad et al. (2018) could not determine how far the observed average cold ion distribution is above escape energy.

Reversely, we may consider the effect on the escape response if instead the required escape energy was higher, as is the case at Venus. Here, Lundin et al. (2011) found that ions in the induced magnetotail are gravitationally bound up to altitudes of several thousand kilometers, as shown in Fig. 15. Naturally, if these ions are not additionally accelerated they fall back to the planet, resulting in the observed return flows. There are no systematic studies of coupling efficiencies with Venus, however, if we assume that the trends at Mars (Figs. 13 and 14) are representative of induced magnetospheres in general, we should expect for Venus O^+ escape a weak though positive dependence on solar wind p_{dyn} and an inverse dependence on solar EUV, consistent with rates reported by Kollmann et al. (2016) and Masunaga et al. (2019), cf. Figs. 8 and 9.

5 Discussion, Conclusions, and Implications

5.1 The Roles of Gravity, Energy Transfer, and Ion Supply

From an initial standpoint, it could seem counterintuitive that Mars, being lighter than both Venus and Earth, is less sensitive to solar wind. After all, the same increase in energy transfer could power a larger increase in ion escape from Mars than from the Venus or Earth. This may seem more intuitive if we consider even lighter objects, such as comets. A comet's coma is equivalent to the upper atmosphere or exosphere of a planet, with the notable distinction that nearly the entire neutral distribution is above escape energy due to the low gravity, and thus that will also be the case for any produced ions. Calculating the ion escape rate for such an object is trivial, the ion escape rate out of any volume around the comet will be equal to the total ion production rate inside the volume, neglecting losses due to recombination. The solar wind can supply more energy, or less, which will accelerate ions to higher energies, but will make no difference for the ion escape rate. In effect, cometary ion escape is entirely supply-limited. In this regard, ion escape from Mars appears to behave much like a comet, i.e. the required escape energy is small enough that under the observed range of upstream solar wind and EUV conditions, all the energy required to maintain the current rate of escape is already provided. While there was little observational evidence for such a supply-limited Martian escape regime, the concept has previously been suggested in relation to modelled wave-heating-driven ion escape (Ergun et al. 2006; Andersson et al. 2010).

In contrast, ion escape from Venus and Earth appears limited by energy transfer from the solar wind. Indeed, at the Earth the escaping fluxes have been observed to increase in direct response to the downward Poynting flux with strong correlation (Strangeway et al. 2005). The lower sensitivity of Venus to solar wind variations appears, at least hypothetically, caused by the corresponding decrease in solar wind coupling efficiency with p_{dyn} inferred from studies on Mars. Similarly, the diverging ion escape response to solar EUV appears to be due to the effect of EUV on ionospheric conductivity, and appears to have opposite effects on solar wind coupling efficiency for non-magnetized and magnetized planets, although Joule-heating rates may also differ. The relative effects of upstream and planetary properties in relation to the inferred states of ion escape are summarized in Fig. 16.

Naturally, the locations of the domains in Fig. 16 are only relative. Hopefully, future studies will constrain and quantify the supply and energy-transfer rates over an expanded range of upstream conditions for each planet and deconvolute the combined effects of the mutually correlated upstream parameters. For example, if Mars is subjected to extremely high EUV conditions and/or tenuous solar wind – will we observe Venus-like return flows as the solar wind interaction transitions to an energy-limited state? Analogous comparisons may also be made for Venus and Earth under extremely strong solar wind conditions if sufficient coverage becomes available with the arrival of future spacecraft. In the present, such conditions might only be available for numerical models of the interaction (e.g. MHD, Particle-in-cell, hybrid), which can apply varying ranges of upstream conditions including the extremes and could be used to estimate the likelihood of observing a state transition.

5.2 Solar Wind Driven Ion Escape Is Not Necessary to Explain the Loss of Mars' Atmosphere

The earliest robotic missions to Mars discovered that the Martian atmosphere is thin, dry, and that the planet lacks a global magnetic dipole, thus it stood to reason that the close

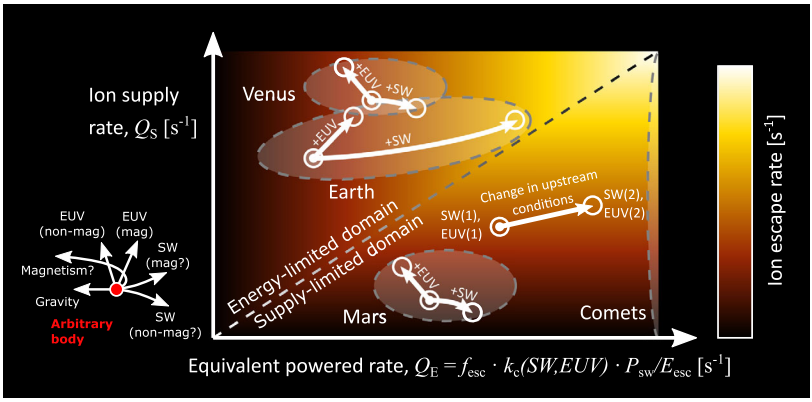

Fig. 16 Domain-space of relative ion supply and solar wind energy transfer in relation to the ion escape rate. The locations of shaded areas represent the ranges typical for each planet and are roughly inferred from the observed dependencies in heavy ion escape and coupling on upstream conditions. In the energy-limited domain the escape rate is insensitive to changes in ion supply (i.e. EUV flux), in the supply-limited domain the escape rate is instead insensitive to changes in energy transfer. However, if the planetary properties were different the domains would shift under the same conditions, e.g. increased gravity would move an otherwise equivalent Mars-like planet to the left (E_{esc} increases), with little effect on the escape rate if all else remains equal, until it were to cross into the energy-limited domain. The arrows indicate the expected movement in the domain-space due to a change in the respective upstream parameter, e.g. a relative change in solar wind has a much stronger effect on Earth compared to Venus due to a near-constant coupling coefficient (k_c) without dependence on p_{dyn}, whereas Venus (like Mars) is expected to decrease coupling with increased p_{dyn}

interaction with the solar wind may have been responsible for the loss of the early atmosphere. However, Mars gravity is just low enough that hydrogen can escape thermally and oxygen can escape in exothermic reactions. In particular, the solar EUV-driven dissociative recombination reaction $O_2^+ + e^- \rightarrow 2O + E$, where E is the energy released in the reaction, can produce oxygen atoms with individual kinetic energies up to about 5 eV for the highest vibrational states of O_2^+ (Fox and Hać 2009; Futaana et al. 2011). This energy is sufficient to escape the relatively shallow Martian gravity well, yet not sufficient to facilitate oxygen escape from Earth or Venus. Recent empirical estimates of photochemical hot O escape rates are in the range of a few 10^{25} s^{-1} up to 10^{26} s^{-1} (Lillis et al. 2017; Rahmati et al. 2018). Scaling photochemical escape rates 3.5 Ga back in time, Lillis et al. (2017) found that photochemical escape alone may account for up to ~1 bar of lost atmosphere. The mystery of the lost Martian atmosphere may thus have a resolution that does not rely on the solar wind as the main driver for the loss of the early atmosphere.

Yet, solar wind driven ion escape has also contributed to the loss of the early Martian atmosphere. A recent empirical estimate of the total amount of atmosphere lost through ion escape over the past 4 Ga is small, less than ~0.01 bar (Ramstad et al. 2018), however, such a simplistic extrapolation assumes a similar state of the Mars–solar wind interaction. The presence of the strong crustal magnetic fields in the most ancient areas of Mars' crust strongly indicate the presence of an early global Martian magnetic dipole. This global dipole appears to have collapsed around 4.2 Ga ago as evidenced from the demagnetization of young large impact basins such as Argyre, Hellas, Isidis and Utopia (Lillis et al. 2008). Nevertheless, if the recent tentative evidence for a later dipole around 3.7 Ga ago prove valid (Mittelholz et al. 2020), extrapolation beyond 3.7 Ga may require a model that also accounts for the transient magnetized state of the planet.

In addition, unlike at Earth, where ion escape is the only effective mechanism for removing the heavier constituents of the atmosphere, the presence and strength of an early Martian magnetic field may also have had secondary effects on neutral escape from the planet due to its lower gravity. In particular, a global magnetic field could have significantly reduced the effects of solar wind-driven sputtering of neutral particles. This sputtering may occur due to a small fraction of solar wind protons and Hydrogen Energetic Neutral Particles (H-ENAs) which precipitate into the upper atmosphere with energies on the order of 1 keV (Halekas et al. 2015a; Shematovich and Kalinicheva 2020). Additionally, a small fraction of heavy ions produced by ionization of the Martian hot oxygen corona, which is immersed in the solar wind, are accelerated to energies on the order of 10's keV by solar wind pick-up (cf. Sects. 2.2 and 4.1). Some fraction of these energized particles precipitate into the upper atmosphere, collisionally transferring sufficient momentum to neutral particles that a fraction undergo sputtered escape. An expansive magnetosphere prevents solar wind pick up and thus also at least some sputtering. However, the effectiveness of the sputtering process is not well understood due to the difficulties in measuring the relatively low energy ($<$10's eV) and low flux of sputtered neutrals, thus sputtering rates have relied on models, with estimated sputtered oxygen rates in the range of orders 10^{23-25} s^{-1} (Wang et al. 2015; Shematovich and Kalinicheva 2020).

5.3 The Magnetosphere Does Not Protect the Earth's Atmosphere

To answer the question of whether any particular planetary property protects the atmosphere, we could consider either or both of two potential qualifiers:

1. Does it lower the escape rate under the same upstream conditions?
2. Does it decrease the sensitivity to external forcing factors (solar wind, EUV, IMF)?

Regarding the magnetic field of the Earth, we may find the answer to both questions in Fig. 8 by comparing the ion escape rates from Venus and Earth, which have similar gravity wells and thus also roughly equivalent escape energies. Under similar solar wind conditions the ion escape rate from Earth is roughly equal to, or higher, than the ion escape rate from Venus, by about an order of magnitude at the highest p_{dyn}. Though, in this comparison the EUV levels differ, and since the respective EUV dependencies are opposite, our comparison (and answer) will depend on whether we compare the two under typical upstream conditions at Venus' orbit or at Earth's orbit. If we consider Venus low-EUV conditions as representative of high EUV conditions for Earth in its natural orbit, though without an intrinsic dipole, then the effect of the dipole is either negligible or increases the escape rate (depending on which E_{mot}-case at Venus we compare with as specified by (Masunaga et al. 2019)). If indeed the heavy ion escape process is energy-limited at both planets (Strangeway et al. 2005; Persson et al. 2020), it follows that the Earth's intrinsic magnetosphere is facilitating a higher rate of energy transfer from the solar wind to the atmospheric ions. This may be explained by the inflated obstacle to the solar wind imposed by the magnetic pressure from Earth's intrinsic magnetosphere as the large cross-section area intersects many times the amount of solar wind energy flux compared to the Venusian induced magnetosphere, when subject to the same upstream solar wind parameters.

The 2nd qualifier question is more straightforward to answer; no. Clearly, ion escape from Earth is much more sensitive to solar wind variations than both Venus and Mars, and neutral escape processes are not effective due to Earth's high gravity. Additionally, the dipole also makes ion escape from Earth escape positively sensitive to solar EUV, which otherwise decreases ion escape from Venus' similar gravity well. The answer to this question also

implies that the magnetic dipole has not protected the Earth's atmosphere during its evolutionary history, as the solar wind and EUV in the early solar system were more intense compared to the present (Ribas et al. 2005; Tu et al. 2015; Wood 2006).

It is possible that the dependence could be less steep if escape through the plasma sheet was included for the Earth in Fig. 8, such that the escape rate would be higher for low p_{dyn}, however, this would instead invalidate the 1st qualifier. We should also consider that there are several aspects of early solar and planetary conditions that not well constrained, such as e.g. the occurrence of super-flares and super-extreme CMEs, the magnetic moments and the composition of the upper atmospheres of the early planets. For example, geological evidence suggests that the early ($\sim$3.5 Ga ago) geodynamo was weaker than in the present (Tarduno et al. 2010), therefore the trends observed in the present can only apply to the present, at least directly. To estimate the escape response under external or intrinsic conditions that are not available in the present-day solar system requires either a method of extrapolation or accurate models of the escape process.

5.4 Are Planetary Dynamos Necessary for the Long-Term Stability of Planetary Atmospheres?

Planetary dynamos exhibit a wide range of magnetic moments. Compared to its unmagnetized counterparts, the Earth's geodynamo appears to decrease solar wind coupling with the ionosphere during weak solar wind and low EUV levels, and to increase coupling during strong solar wind and high EUV levels. It thus seems reasonable that the protective effects of a dynamo depends on some relation of the planets magnetic moment and the upstream parameters. Under a particular set of solar wind, IMF and EUV parameters, a sufficiently strong intrinsic magnetic dipole may protect the atmosphere by decreasing solar wind coupling, however a weak dipole may increase coupling and rate of atmospheric escape.

Unfortunately Earth is the only terrestrial globally magnetized planet with an atmosphere available in the solar system for in-situ studies. However, some studies have modelled the interaction of the solar wind with the solar system's terrestrial planets for various unnatural magnetic field strengths. Cnossen et al. (2012) used a magnetohydrodynamics (MHD) model to simulate the solar wind magnetosphere interaction for 5 different dipole moments, each under three different solar EUV levels, and found an increase in ionospheric coupling with the solar wind for weak dipole strengths, which peaks at 4×10^{22} A m^2 under low EUV fluxes, and at 6×10^{22} A m^2 for high EUV fluxes (Earth's magnetic moment is 8×10^{22} A m^2 for reference). In their model higher magnetic moments resulted in a gradual reduction of the coupling. Similar modeling efforts have also been made for Mars: Sakai et al. (2018) introduced a weak intrinsic dipole (4×10^{19} A m^2 to an MHD simulation of the Mars-solar wind interaction, finding a $\sim$25 % increase in the escape rate primarily due to an enhancement in O_2^+ fluxes. The increase in O_2^+ fluxes is explained as resulting from increased uplifting of ions from lower altitudes (where O_2^+ is the dominant ion species) due to the introduction of vertical field-lines. Effectively, the added dipole increased the ion supply rate. However, the small size of the Martian magnetosphere creates an interaction with the solar wind that is comparable to, or below, the typical local ion-kinetic scales, which MHD by the nature of the fluid approximation cannot reproduce. Instead, Egan et al. (2019) recently utilized a hybrid model (ions modeled as kinetic particles, electrons as a magnetized fluid) to simulate the Mars-solar wind interaction for a range of intrinsic dipole moments from completely unmagnetized up to 6×10^{19} A m^2. They find that the Martian escape rate would increase with dipole strength until a peak is reached at 2×10^{19} A m^2. In their model the escape rate initially increases despite a reduction in the energy transfer due to the expansion of

the polar cap, effectively increasing the ion supply rate. With higher dipole strengths the intrinsic magnetopause expands beyond the IMB, resulting in trapping of outflowing ions on closed field-lines, forming a plasmasphere. In other words, further increase of the dipole strength effectively reduces the transport efficiency which lowers the escape rate, despite a largely unaffected energy transfer rate, which this does not affect the escape rate in the supply-limited Martian system.

While such modeling efforts are only beginning to explore the influence of magnetization on atmospheric escape, the results of these recent studies are largely consistent with measurements at Earth, Venus, and Mars. While there is still the need to explore the efficacy of solar wind driven neutral escape processes, such as sputtering at low-mass planets, it is clear that the presently available evidence does not support the current paradigm, which views intrinsic magnetospheres as planetary shields that prevent atmospheric escape. In contrast, *an intrinsic magnetic field is not necessarily needed to protect a planet's atmosphere from solar and stellar winds*, rather the presence of a dipole appears to increase the rate of ion escape unless the field strength is strong enough in relation to the upstream stellar wind and EUV flux from the host star, and the gravity of the planet. In light of what has been learnt from the past few decades of measurements in the solar system, it is clear that the current paradigm does not conform to the evidence and a more nuanced view of the intrinsic magnetic field's role is required for the new one.

Acknowledgements We thank William K. Peterson for helpful feedback on the initial manuscript. We are thankful for the insightful comments from Janet G. Luhmann and an anonymous reviewer, which solidified the broad scope of the paper. We also thank Kei Masunaga for providing detailed information on the upstream conditions included in the study by Masunaga et al. (2019). R.R. is supported by NASA's Mars Exploration Program through its support of the MAVEN mission to Mars.

References

S.I. Akasofu, Energy coupling between the solar wind and the magnetosphere. Space Sci. Rev. **28**(2), 121–190 (1981). https://doi.org/10.1007/BF00218810

H. Akbari, L. Andersson, W.K. Peterson, J. Espley, M. Benna, R. Ergun, Ambipolar electric field in the Martian ionosphere: MAVEN measurements. J. Geophys. Res. **124**, 4518–4524 (2019). https://doi.org/10.1029/2018JA026325

H. Alfvén, On the theory of comet tails. Tellus **9**(1), 92–96 (1957). https://doi.org/10.3402/tellusa.v9i1.9064

L. Andersson, W.K. Peterson, K.M. McBryde, Estimates of the suprathermal O^+ outflow characteristic energy and relative location in the auroral oval. Geophys. Res. Lett. **32**, L09104 (2005). https://doi.org/10.1029/2004GL021434

L. Andersson, R.E. Ergun, A.I.F. Stewart, The combined atmospheric photochemistry and ion tracing code: Reproducing the Viking Lander results and initial outflow results. Icarus **206**, 120–129 (2010). https://doi.org/10.1016/j.icarus.2009.07.009

M. André, Previously hidden low-energy ions: A better map of near-Earth space and the terrestrial mass balance. Phys. Scr. **90**, 128005 (2015). https://doi.org/10.1088/0031-8949/90/12/128005

S. Barabash et al., The Analyzer of Space Plasmas and Energetic Atoms (ASPERA-3) for the Mars express mission. Space Sci. Rev. **126**, 113–164 (2006). https://doi.org/10.1007/s11214-006-9124-8

S. Barabash et al., The Analyzer of Space Plasmas and Energetic Atoms (ASPERA-4) for the Venus express mission. Planet. Space Sci. **55**, 1772–1792 (2007a). https://doi.org/10.1016/j.pss.2007.01.014

S. Barabash et al., The loss of ions from Venus through the plasma wake. Nature **450**, 650–653 (2007b). https://doi.org/10.1038/nature06434

S. Barabash, A. Fedorov, R. Lundin, J.-A. Sauvaud, Martian atmospheric erosion rates. Science **315**(5811), 501–503 (2007c). https://doi.org/10.1126/science.1134358

W. Baumjohann, M. Blanc, A. Fedorov, K.-H. Glassmeier, Current systems in planetary magnetospheres and ionospheres. Space Sci. Rev. **52**, 99–154 (2010). https://doi.org/10.1007/s11214-010-9629-z

A.V. Bogdanov, O.L. Vaisberg, N.P. Kalinin, V.N. Smirnov, Gas exchange between the upper atmosphere of Mars and the solar wind. Dokl. Akad. Nauk **225**(6), 1284–1287 (1975) (in Russian)

L.H. Brace, W.T. Kasprzak, H.A. Taylor, R.F. Theis, C.T. Russell, A. Barnes, J.D. Mihalov, D.M. Hunten, The ionotail of Venus: Its configuration and evidence for ion escape. J. Geophys. Res. Space Phys. **92**(A1), 15–26 (1987). https://doi.org/10.1029/JA092iA01p00015

D.A. Brain et al., The spatial distribution of planetary ion fluxes near Mars observed by MAVEN. Geophys. Res. Lett. **42**, 9142–9148 (2015). https://doi.org/10.1002/2015GL065293

E. Carlsson et al., Mass composition of the escaping plasma at Mars. Icarus **182**, 320–328 (2006). https://doi.org/10.1016/j.icarus.2005.09.020

S. Chapman, V.C.A. Ferraro, A new theory of magnetic storms. Terr. Magn. Atmos. Electr. **36**(2), 77–97 (1931)

I. Cnossen, A.D. Richmond, M. Wiltberger, The dependence of the coupled magnetosphere–ionosphere–thermosphere system on the Earth's magnetic dipole moment. J. Geophys. Res. Space Phys. **117**, A05302 (2012). https://doi.org/10.1029/2012JA017555

A.J. Coates et al., Cassini in Titan's tail: CAPS observations of plasma escape. J. Geophys. Res. Space Phys. **117**, A05324 (2012). https://doi.org/10.1029/2012JA017595

G. Collinson et al., The electric wind of Venus: A global and persistent "polar wind"-like ambipolar electric field sufficient for the direct escape of heavy ionospheric ions. Geophys. Res. Lett. **43**, 5926–5934 (2016). https://doi.org/10.1002/2016GL068327

S.W.H. Cowley, Magnetosphere-ionosphere interactions: A tutorial review, in *Magnetospheric Current Systems*, ed. by S. Ohtani. Geophysical Monograph Series, vol. 118 (2000), pp. 91–106

C.M. Cully, E.F. Donovan, A.W. Yau, G.G. Arkos, Akebono/suprathermal mass spectrometer observations of low-energy ion outflow: Dependence on magnetic activity and solar wind conditions. J. Geophys. Res. Space Phys. **108**(A2), 1093 (2003). https://doi.org/10.1029/2001JA009200

G.A. DiBraccio et al., The twisted configuration of the Martian magnetotail: MAVEN observations. Geophys. Res. Lett. **45**, 4559–4568 (2018). https://doi.org/10.1029/2018GL077251

C. Diéval, G. Stenberg, H. Nilsson, S. Barabash, A statistical study of proton precipitation onto the Martian upper atmosphere: Mars Express observations. J. Geophys. Res. Space Phys. **118**, 1972–1983 (2013). https://doi.org/10.1002/jgra.50229

Y. Dong, X. Fang, D.A. Brain, J.P. McFadden, J.S. Halekas, J.E.P. Connerney, F. Eparvier, L. Andersson, D. Mitchell, B.M. Jakosky, Seasonal variability of Martian ion escape through the plume and tail from MAVEN observations. J. Geophys. Res. Space Phys. **122**, 4009–4022 (2017). https://doi.org/10.1002/2016JA023517

E. Dubinin, K. Sauer, R. Lundin, O. Norberg, J.G. Trotignon, K. Schwingenschuh, M. Delva, W. Riedler, Plasma characteristics of the boundary layer in the Martian magnetosphere. J. Geophys. Res. Space Phys. **101**(A12), 27061–27075 (1996). https://doi.org/10.1029/96JA02021

E. Dubinin et al., Structure and dynamics of the solar wind/ionosphere interface on Mars: MEX-ASPERA-3 and MEX-MARSIS observations. Geophys. Res. Lett. **35**, L11103 (2008). https://doi.org/10.1029/2008GL033730

E. Dubinin, M. Fraenz, J. Woch, T.L. Zhang, Y. Wei, A. Fedorov, S. Barabash, R. Lundin, Toroidal and poloidal magnetic fields at Venus. Venus Express observations. Planet. Space Sci. **87**, 19–29 (2013). https://doi.org/10.1016/j.pss.2012.12.003

E. Dubinin, M. Fraenz, M. Pätzold, J. McFadden, J.S. Halekas, G.A. DiBraccio, J.E.P. Connerney, F. Eparvier, D. Brain, B.M. Jakosky, O. Vaisberg, L. Zelenyi, Effects of solar irradiance on the upper ionosphere and oxygen ion escape at Mars: MAVEN observations. J. Geophys. Res. Space Phys. **122**, 7142–7152 (2017). https://doi.org/10.1002/2017JA024126

N.J.T. Edberg, D.A. Brain, M. Lester, S.W.H. Cowley, R. Modolo, M. Fränz, S. Barabash, Plasma boundary variability at Mars as observed by Mars Global Surveyor and Mars Express. Ann. Geophys. **27**, 3537–3550 (2009). https://doi.org/10.5194/angeo-27-3537-2009

N.J.T. Edberg, H. Nilsson, A.O. Williams, M. Lester, S.E. Milan, S.W.H. Cowley, M. Fränz, S. Barabash, Y. Futaana, Pumping out the atmosphere of Mars through solar wind pressure pulses. Geophys. Res. Lett. **37**, L03107 (2010). https://doi.org/10.1029/2009GL041814

N.J.T. Edberg, H. Nilsson, Y. Futaana, G. Stenberg, M. Lester, S.W.H. Cowley, J.G. Luhmann, T.R. McEnulty, H.J. Opgenoorth, A. Fedorov, S. Barabash, T.L. Zhang, Atmospheric erosion of Venus during stormy space weather. J. Geophys. Res. **116**, A09308 (2011). https://doi.org/10.1029/2011JA016749

C.S. Edwards, B.L. Ehlmann, Carbon sequestration on Mars. Geology **43**(10), 863–866 (2015). https://doi.org/10.1130/G36983.1

H. Egan, R. Jarvinen, Y. Ma, D. Brain, Planetary magnetic field control of ion escape from weakly magnetized planets. Mon. Not. R. Astron. Soc. **488**, 2108–2120 (2019). https://doi.org/10.1093/mnras/stz1819

R.E. Ergun, L. Andersson, W.K. Peterson, D. Brain, G.T. Delory, D.L. Mitchell, R.P. Lin, A.W. Yau, Role of plasma waves in Mars' atmospheric loss. Geophys. Res. Lett. **33**, L14103 (2006). https://doi.org/10.1029/2006GL025785

K. Fan, M. Fränz, Y. Wei, J. Cui, Z. Rong, L. Chai, E. Duninin, Deflection of global ion flow by the Martian crustal magnetic fields. Astrophys. J. Lett. **898**, L54 (2020). https://doi.org/10.3847/2041-8213/aba519

A. Fedorov et al., Comparative analysis of Venus and Mars magnetotails. Planet. Space Sci. **56**, 812–817 (2008). https://doi.org/10.1016/j.pss.2007.12.012

A. Fedorov, S. Barabash, J.A. Sauvaud, Y. Futaana, T.L. Zhang, R. Lundin, R. Ferrier, Measurements of the ion escape rates from Venus for solar minimum. J. Geophys. Res. **116**, A07220 (2011). https://doi.org/10.1029/2011JA016427

I. Finch, M. Lockwood, Solar wind-magnetosphere coupling functions on timescales of 1 day to 1 year. Ann. Geophys. **25**(2), 495–506 (2007). https://doi.org/10.5194/angeo-25-495-2007

C.M. Fowler et al., MAVEN observations of solar wind-driven magnetosonic waves heating the Martian dayside ionosphere. J. Geophys. Res. Space Phys. **123**, 4129–4149 (2018). https://doi.org/10.1029/2018JA025208

J.L. Fox, A.B. Hać, Photochemical escape of oxygen from Mars: A comparison of the exobase approximation to a Monte Carlo method. Icarus **204**, 527–544 (2009). https://doi.org/10.1016/j.icarus.2009.07.005

L.A. Frank, K.L. Ackerson, D.M. Yeager, Observations of atomic oxygen (O^+) in the Earth's magnetotail. J. Geophys. Res. **82**(1), 129–134 (1977). https://doi.org/10.1029/JA082i001p00129

S.F. Fung, R.A. Hoffman, A search for parallel electric fields by observing secondary electrons and photoelectrons in the low-altitude auroral zone. J. Geophys. Res. **96**(A3), 3533–3548 (1991). https://doi.org/10.1029/90JA02244

Y. Futaana, J.Y. Chaufray, H.T. Smith, P. Garnier, H. Lichtenegger, M. Delva, H. Gröller, A. Mura, Exospheres and energetic neutral atoms of Mars, Venus and Titan. Space Sci. Rev. **162**, 213–266 (2011). https://doi.org/10.1007/s11214-011-9834-4

N.Yu. Ganushkina, M.W. Liemohn, S. Dubyagin, Current systems in the Earth's magnetosphere. Rev. Geophys. **56**, 309–332 (2018). https://doi.org/10.1002/2017RG000590

J.S. Halekas et al., MAVEN observations of solar wind hydrogen deposition in the atmosphere of Mars. Geophys. Res. Lett. **42**, 8901–8909 (2015a). https://doi.org/10.1002/2015GL064693

J.S. Halekas, E.R. Taylor, G. Dalton, G. Johnson, D.W. Curtis, J.P. McFadden, D.L. Mitchell, R.P. Lin, B.M. Jakosky, The solar wind ion analyzer for MAVEN. Space Sci. Rev. **195**, 125–151 (2015b). https://doi.org/10.1007/s11214-013-0029-z

T. Hara et al., MAVEN observations on a hemispheric asymmetry of precipitating ions toward the Martian upper atmosphere according to the upstream solar wind electric field. J. Geophys. Res. Space Phys. **122**, 1083–1101 (2017). https://doi.org/10.1002/2016JA023348

B.M. Jakosky et al., MAVEN observations of the response of Mars to an interplanetary coronal mass ejection. Science **350**(6261), aad0210-1 (2015). https://doi.org/10.1126/science.aad0210

A. Keiling, J.R. Wygant, C.A. Cattell, F.S. Mozer, C.T. Russell, The global morphology of wave Poynting flux: Powering the aurora. Science **299**(5605), 383–386 (2003). https://doi.org/10.1126/science.1080073

L.M. Kistler et al., Escape of O^+ through the distant tail plasma sheet. Geophys. Res. Lett. **37**, L21101 (2010). https://doi.org/10.1029/2010GL045075

D.M. Klumpar et al., The time-of-flight energy, angle, mass spectrograph (TEAMS) experiment for FAST, in *The FAST Mission* (2001), pp. 197–219. ISBN: 978-94-010-3847-8

P. Kollmann, P.C. Brandt, G. Collinson, Z.J. Rong, Y. Futaana, T.L. Zhang, Properties of planetward ion flows in Venus' magnetotail. Icarus **274**, 73–82 (2016). https://doi.org/10.1016/j.icarus.2016.02.053

H. Lammer, *Origin and Evolution of Planetary Atmospheres* (Springer, Berlin, 2013). ISBN: 978-3-642-32086-6. https://doi.org/10.1007/978-3-642-32087-3

O.W. Lennartsson, H.L. Collin, Solar wind control of Earth's H^+ and O^+ outflow rates in the 15-eV to 33-keV energy range. J. Geophys. Res. **109**(A12212) (2004). https://doi.org/10.1029/2004JA010690

K. Li, Y. Wei, M. André, A. Eriksson, S. Haaland, E.A. Kronberg, H. Nilsson, L. Maes, Z.J. Rong, W.X. Wan, Cold ion outflow modulated by the solar wind energy input and tilt of the geomagnetic dipole. J. Geophys. Res. Space Phys. **122**(10), 10658–10668 (2017). https://doi.org/10.1002/2017JA024642

R.J. Lillis, H.V. Frey, M. Manga, Rapid decrease in Martian crustal magnetization in the Noachian era: Implications for the dynamo and climate of early Mars. Geophys. Res. Lett. **35**, L14203 (2008). https://doi.org/10.1029/2008GL034338

R.J. Lillis et al., Photochemical escape of oxygen from Mars: First results from MAVEN in situ data. J. Geophys. Res. Space Phys. **122**, 3815–3836 (2017). https://doi.org/10.1002/2016JA023525

M. Lockwood, Does adding solar wind Poynting flux improve the optimum solar wind-magnetosphere coupling function? J. Geophys. Res. Space Phys. **124**, 5498–5515 (2019). https://doi.org/10.1029/2019JA026639

R. Lundin, B. Hultqvist, S. Olsen, R. Pellinen, I. Liede, A. Zakharov, E. Dubinin, N. Pissarenko, The ASPERA experiment on the Soviet Phobos spacecraft, in *Solar System Plasma Physics*. American Geophysical Union Monograph Series, vol. 54 (1985), pp. 417–424. ISBN: 9780875900742

R. Lundin et al., ASPERA/Phobos measurements of the ion outflow from the Martian ionosphere. Geophys. Res. Lett. **17**(6), 873–876 (1990). https://doi.org/10.1029/GL017i006p00873

R. Lundin, S. Barabash, A. Fedorov, M. Holmström, H. Nilsson, J.A. Sauvaud, M. Yamauchi, Solar forcing and planetary ion escape from Mars. Geophys. Res. Lett. **35**, L09203 (2008a). https://doi.org/10.1029/2007GL032884

R. Lundin, S. Barabash, M. Holmström, H. Nilsson, M. Yamauchi, M. Fraenz, E.M. Dubinin, A comet-like escape of ionospheric plasma from Mars. Geophys. Res. Lett. **35**, L18203 (2008b). https://doi.org/10.1029/2008GL034811

R. Lundin, S. Barabash, Y. Futaana, J.A. Sauvaud, A. Fedorov, H. Perez-de-Tejada, Ion flow and momentum transfer in the Venus plasma environment. Icarus **215**, 751–758 (2011). https://doi.org/10.1016/j.icarus.2011.06.034

R. Lundin, S. Barabash, M. Holmström, H. Nilsson, Y. Futaana, R. Ramstad, M. Yamauchi, E. Dubinin, M. Fraenz, Solar cycle effects on the ion escape from Mars. Geophys. Res. Lett. **40**, 6028–6032 (2013). https://doi.org/10.1002/2013GL058154

L.R. Lyons, T.W. Speiser, Ohm's law for a current sheet. J. Geophys. Res. **90**(A9), 8543–8546 (1985). https://doi.org/10.1029/JA090iA09p08543

N. Mangold, D. Baratoux, O. Witasse, T. Encrenaz, C. Sotin, Mars: A small terrestrial planet. Astron. Astrophys. Rev. **24**(1), 15 (2016). https://doi.org/10.1007/s00159-016-0099-5

K. Masunaga, Y. Futaana, M. Persson, S. Barabash, T.L. Zhang, Z.J. Rong, A. Fedorov, Effects of the solar wind and the solar EUV flux on O+ escape rates from Venus. Icarus **321**, 379–387 (2019). https://doi.org/10.1016/j.icarus.2018.11.017

D.J. McComas, H.E. Spence, C.T. Russell, M.A. Saunders, The average magnetic field draping and consistent plasma properties of the Venus magnetotail. J. Geophys. Res. Space Phys. **91**, 7939–7953 (1986). https://doi.org/10.1029/JA091iA07p07939

D.J. McComas et al., Pluto's interaction with the solar wind. J. Geophys. Res. Space Phys. **121**, 4232–4246 (2016). https://doi.org/10.1002/2016JA022599

J.P. McFadden et al., MAVEN SupraThermal and Thermal Ion Composition (STATIC) instrument. Space Sci. Rev. **195**, 199–256 (2015). https://doi.org/10.1007/s11214-015-0175-6

S.E. Milan, Both solar wind-magnetosphere coupling and ring current intensity control of the size of the auroral oval. Geophys. Res. Lett. **36**, L18101 (2009). https://doi.org/10.1029/2009GL039997

A. Mittelholz, C.L. Johnson, J.M. Feinberg, B. Langlais, R.J. Phillips, Timing of the Martian dynamo: New constraints for a core field 4.5 and 3.7 Ga ago. Sci. Adv. **6**(18), eaba0513 (2020). https://doi.org/10.1126/sciadv.aba0513

T.E. Moore, J.L. Horwitz, Stellar ablation of planetary atmospheres. Rev. Geophys. **45**, RG3002 (2007). https://doi.org/10.1029/2005RG000194

H. Nilsson, E. Carlsson, D.A. Brain, M. Yamauchi, M. Holmström, S. Barabash, R. Lundin, Y. Futaana, Ion escape from Mars as a function of solar wind conditions: A statistical study. Icarus **206**, 40–49 (2010). https://doi.org/10.1016/j.icarus.2009.03.006

H. Nilsson, N.J.T. Edberg, G. Stenberg, S. Barabash, M. Holmström, Y. Futaana, R. Lundin, A. Fedorov, Heavy ion escape from Mars, influence from solar wind conditions and crustal magnetic fields. Icarus **215**, 475–484 (2011). https://doi.org/10.1016/j.icarus.2011.08.003

H. Nilsson, I.A. Bargouthi, R. Slapak, A.I. Eriksson, M. André, Hot and cold ion outflow: Spatial distributions of ion heating. J. Geophys. Res. **117**, A11201 (2012a). https://doi.org/10.1029/2012JA017974

H. Nilsson, G. Stenberg, Y. Futaana, M. Holmström, S. Barabash, R. Lundin, N.J.T. Edberg, A. Fedorov, Ion distributions in the vicinity of Mars: Signatures of heating and acceleration processes. Earth Planets Space **64**, 135–148 (2012b). https://doi.org/10.5047/eps.2011.04.011

T. Nordström, G. Stenberg, H. Nilsson, S. Barabash, T.L. Zhang, Venus ion outflow estimates at solar minimum: Influence of reference frames and disturbed solar wind conditions. J. Geophys. Res. Space Phys. **118**, 3592–3601 (2013). https://doi.org/10.1002/jgra.50305

S. Ohtani, S. Wing, V.G. Merkin, T. Higuchi, Solar cycle dependence of nightside field-aligned currents: Effects of dayside ionospheric conductivity on the solar wind-magnetosphere-ionosphere coupling. J. Geophys. Res. Space Phys. **119**, 322–334 (2014). https://doi.org/10.1002/2013JA019410

E.N. Parker, Dynamics of the interplanetary gas and magnetic fields. Astrophys. J. **128**, 664–676 (1958). https://doi.org/10.1086/146579

M. Persson, Y. Futaana, A. Fedorov, H. Nilsson, M. Hamrin, S. Barabash, H^+/O^+ escape rate ratio in the Venus magnetotail and its dependence on the solar cycle. Geophys. Res. Lett. **45**, 10805–10811 (2018). https://doi.org/10.1029/2018GL079454

M. Persson, Y. Futaana, R. Ramstad, K. Masunaga, H. Nilsson, M. Hamrin, A. Fedorov, S. Barabash, The Venusian atmospheric oxygen ion escape: Extrapolation to the early solar system. J. Geophys. Res., Planets **125**, e2019JE006336 (2020). https://doi.org/10.1029/2019JE006336

W.K. Peterson, H.L. Collin, A.W. Yau, O.W. Lennartsson, Polar/toroidal imaging mass-angle spectrograph observations of suprathermal ion outflow during solar minimum conditions. J. Geophys. Res. **106**(A4), 6059–6066 (2001). https://doi.org/10.1029/2000JA003006

J.L. Phillips, J.G. Luhmann, C.T. Russell, K.R. Moore, Finite Larmor radius effect on ion pickup at Venus. J. Geophys. Res. **92**(A9), 9920–9930 (1987). https://doi.org/10.1029/JA092iA09p09920

A. Rahmati, D.E. Larson, T.E. Cravens, R.J. Lillis, J.S. Halekas, J.P. McFadden, D.L. Mitchell, E.M.B. Thiemann, J.E.P. Connerney, P.A. Dunn, C.O. Lee, F.G. Eparvier, G.A. DiBraccio, J.R. Espley, J.G. Luhmann, C. Mazelle, B.M. Jakosky, Seasonal variability of neutral escape from Mars as derived from MAVEN pickup ion observations. J. Geophys. Res., Planets **123**, 1192–1202 (2018). https://doi.org/10.1029/2018JE005560

R.M. Ramirez, A warmer and wetter solution for early Mars and the challenges with transient warming. Icarus **297**, 71–82 (2017). https://doi.org/10.1016/j.icarus.2017.06.025

R.M. Ramirez, R. Kopparapu, M.E. Zugger, T.D. Robinson, R. Freedman, J.F. Kasting, Warming early Mars with CO_2 and H_2. Nat. Geosci. **7**(1), 59–63 (2014). https://doi.org/10.1038/NGEO2000

R. Ramstad, Ion escape from Mars: Measurements in the present to understand the past. Doctoral thesis, Umeå University (2017). ISBN: 978-91-982951-3-9, ISSN: 0284-1703

R. Ramstad, Y. Futaana, S. Barabash, H. Nilsson, S.M. del Campo B, R. Lundin, K. Schwingenschuh, Phobos 2/ASPERA data revisited: Planetary ion escape rate from Mars near the 1989 solar maximum. Geophys. Res. Lett. **40**(1–6), 477–481 (2013). https://doi.org/10.1002/grl.50149

R. Ramstad, S. Barabash, Y. Futaana, H. Nilsson, X.-D. Wang, M. Holmström, The Martian atmospheric ion escape rate dependence on solar wind and solar EUV conditions: 1. Seven years of Mars Express observations. J. Geophys. Res., Planets **120**, 1298–1309 (2015). https://doi.org/10.1002/2015JE004816

R. Ramstad, S. Barabash, Y. Futaana, M. Holmström, Solar wind and EUV dependent models for the sizes and shapes of the Martian plasma boundaries based on Mars Express observations. J. Geophys. Res. Space Phys. **122**, 7279–7290 (2017a). https://doi.org/10.1002/2017JA024098

R. Ramstad, S. Barabash, Y. Futaana, H. Nilsson, M. Holmström, Global Mars–Solar wind coupling and ion escape. J. Geophys. Res. Space Phys. **122**, 8051–8062 (2017b). https://doi.org/10.1002/2017JA024306

R. Ramstad, S. Barabash, Y. Futaana, M. Yamauchi, H. Nilsson, M. Holmström, Mars under primordial solar wind conditions: Mars express observations of the strongest CME detected at Mars under solar cycle #24 and its impact on atmospheric ion escape. Geophys. Res. Lett. **44**, 10805–10811 (2017c). https://doi.org/10.1002/2017GL075446

R. Ramstad, S. Barabash, Y. Futaana, H. Nilsson, M. Holmström, Ion escape from Mars through time: An extrapolation of atmospheric loss based on 10 years of Mars Express measurements. J. Geophys. Res., Planets **123**, 3051–3060 (2018). https://doi.org/10.1029/2018JE005727

R. Ramstad, D.A. Brain, Y. Dong, J. Espley, J. Halekas, B. Jakosky, The current systems of the Martian induced magnetosphere. Nat. Astron. **4**, 979–985 (2020). https://doi.org/10.1038/s41550-020-1099-y

H. Rème, C. Aoustin, J.M. Bosqued, I. Dandouras, B. Lavraud et al., First multispacecraft ion measurements in and near the Earth's magnetosphere with the identical cluster ion spectrometry (CIS) experiment. Ann. Geophys. **19**, 1303–1354 (2001). https://doi.org/10.5194/angeo-19-1303-2001

I. Ribas, E.F. Guinan, M. Güdel, M. Audard, Evolution of solar activity over time and effects on planetary atmospheres. I. High-energy irradiances (1-1700 Å). Astrophys. J. **622**(1), 680–694 (2005). https://doi.org/10.1086/427977

W. Riedler et al., Magnetic fields near Mars: First results. Nature **341**(6243), 604–607 (1989). https://doi.org/10.1038/341604a0

C.T. Russell, J.G. Luhmann, R.C. Elphic, The properties of the low altitude magnetic belt in the Venus ionosphere. Adv. Space Sci. **2**(10), 13–16 (1989). https://doi.org/10.1016/0273-1177(82)90356-8

S. Sakai, K. Seki, N. Terada, H. Shinagawa, T. Tanaka, Y. Ebihara, Effects of a weak intrinsic magnetic field on atmospheric escape from Mars. Geophys. Res. Lett. **45**, 9336–9343 (2018). https://doi.org/10.1029/2018GL079972

M. Saunders, C. Russell, Average dimension and magnetic structure of the distant Venus magnetotail. J. Geophys. Res. **91**(A5), 5589–5604 (1986). https://doi.org/10.1029/JA091iA05p05589

A. Schillings, How does O^+ outflow vary with solar wind conditions? Doctoral thesis, Luleå University (2019). ISBN: 978-91-7790-465-6, ISSN: 1402-1544

A. Schillings, R. Slapak, H. Nilsson, M. Yamauchi, I. Dandouras, L.G. Westerberg, Earth atmospheric loss through the plasma mantle and its dependence on solar wind parameters. Earth Planets Space **71**, 70 (2019). https://doi.org/10.1186/s40623-019-1048-0

K. Seki, R.C. Elphic, M. Hirihara, T. Terasawa, T. Mukai, On atmospheric loss of oxygen from Earth through magnetospheric processes. Science **291**, 1939 (2001). https://doi.org/10.1126/science.1058913

E.G. Shelley, R.G. Johnson, R.D. Sharp, Satellite observations of energetic heavy ions during a geomagnetic storm. J. Geophys. Res. **77**(31), 6104–6110 (1972). https://doi.org/10.1029/JA077i031p06104

V.I. Shematovich, E.S. Kalinicheva, Oxygen atom escape from the Martian atmosphere during proton auroral events. Astron. Rep. **64**(7), 628–635 (2020). https://doi.org/10.1134/S1063772920080089

SILSO World Data Center, The International Sunspot Number, International Sunspot Number Monthly Bulletin and online catalogue (2070–2020). http://www.sidc.be/silso/

R. Slapak, A. Schillings, H. Nilsson, M. Yamauchi, L.G. Westerberg, I. Dandouras, Atmospheric loss from the dayside open polar region and its dependence on geomagnetic activity: Implications for atmospheric escape on evolutionary timescales. Ann. Geophys. **35**, 721–731 (2017). https://doi.org/10.5194/angeo-35-721-2017

R.J. Strangeway, R.E. Ergun, Y.J. Su, C.W. Carlson, R.C. Elphic, Factors controlling ionospheric outflows as observed at intermediate altitudes. J. Geophys. Res. **110**, A03221 (2005). https://doi.org/10.1029/2004JA010829

J.A. Tarduno et al., Geodynamo, solar wind, and magnetopause 3.4 to 3.45 billion years ago. Science **327**(5970), 1238–1240 (2010). https://doi.org/10.1126/science.1183445

P. Tenfjord, N. Østgaard, Energy transfer and flow in the solar wind–magnetosphere–ionosphere system: A new coupling function. J. Geophys. Res. Space Phys. **118**(9), 5659–5672 (2013). https://doi.org/10.1002/jgra.50545

L. Tu, C.P. Johnstone, M. Güdel, H. Lammer, The extreme ultraviolet and X-ray Sun in Time: High-energy evolutionary tracks of a solar-like star. Astron. Astrophys. **577**, L3 (2015). https://doi.org/10.1051/0004-6361/201526146

O.L. Vaisberg, V.N. Smirnov, The Martian magnetotail. Adv. Space Res. **6**(1), 301–314 (1986). https://doi.org/10.1016/0273-1177(86)90046-3

O.L. Vaisberg, V.N. Smirnov, A.N. Omeltchenko, Solar wind interaction with Martian magnetosphere. Preprint IKI, D-252 (1977)

V.M. Vasyliunas, J.R. Kan, G.L. Siscoe, S.I. Akasofu, Scaling relations governing magnetospheric energy transfer. Planet. Space Sci. **30**(4), 359–365 (1982). https://doi.org/10.1016/0032-0633(82)90041-1

G.L. Villanueva, M.J. Mumma, R.E. Novak, H.U. Käufl, P. Hartogh, T. Encrenaz, A. Tokunaga, A. Khayat, M.D. Smith, Strong water isotopic anomalies in the Martian atmosphere: Probing current and ancient reservoirs. Science **348**, 218–221 (2015). https://doi.org/10.1126/science.aaa3630

H. Volland, A semiempirical model of large-scale magnetospheric electric fields. J. Geophys. Res. Space Phys. **78**(1), 171–180 (1973). https://doi.org/10.1029/JA078i001p00171

C. Wang, J.P. Han, H. Li, Z. Peng, J.D. Richardson, Solar wind–magnetosphere energy coupling function fitting: Results from a global MHD simulation. J. Geophys. Res. Space Phys. **119**(8), 6199–6212 (2014). https://doi.org/10.1002/2014JA019834

Y.C. Wang, J.G. Luhmann, X. Fang, F. Leblanc, R.E. Johnson, Y. Ma, W.-H. Ip, Statistical studies on Mars atmospheric sputtering by precipitating pickup O^+: Preparation for the MAVEN mission. J. Geophys. Res., Planets **120**, 34–50 (2015). https://doi.org/10.1002/2014JE004660

Y. Wei, M. Fraenz, E. Dubinin, J. Woch, H. Lühr, W. Wan, Q.G. Zong, T.L. Zhang, Z.Y. Pu, S.Y. Fu, S. Barabash, R. Lundin, I. Dandouras, Enhanced atmospheric oxygen outflow on Earth and Mars driven by a corotating interaction region. J. Geophys. Res. **117**, A03208 (2012). https://doi.org/10.1029/2011JA017340

B.E. Wood, The solar wind and the Sun in the past. Space Sci. Rev. **126**, 3–14 (2006). https://doi.org/10.1007/s11214-006-9006-0

R. Wordsworth, Y. Kalugina, S. Lokshtanov, A. Vigasin, B. Ehlmann, J. Head, C. Sanders, H. Wang, Transient reducing greenhouse warming on early Mars. Geophys. Res. Lett. **44**, 665–671 (2017). https://doi.org/10.1002/2016GL071766

S. Xu, D.L. Mitchell, J.P. McFadden, G. Collinson, Y. Harada, R. Lillis, C. Mazelle, J.E.P. Connerney, Field-aligned potentials at Mars from MAVEN observations. Geophys. Res. Lett. **45**, 10119–10127 (2018). https://doi.org/10.1029/2018GL080136

A.W. Yau, E.G. Shelley, W.K. Peterson, L. Lenchyshyn, Energetic auroral and polar ion outflow at DE 1 altitudes: Magnitude, composition, magnetic activity dependence, and long-term variations. J. Geophys. Res. **90**(A9), 8417–8432 (1985). https://doi.org/10.1029/JA090iA09p08417

A.W. Yau, W.K. Peterson, E.G. Shelley, Quantitative parametrization of energetic ionospheric ion outflow, in *Modeling Magnetospheric Plasma*, vol. 44, ed. by T.E. Moore, J. Waite Jr., T.W. Moorehead, W.B. Hanson (1988), pp. 211–217. https://doi.org/10.1029/GM044p0211

A.W. Yau, T. Abe, W.K. Peterson, The polar wind: Recent observations. J. Atmos. Sol.-Terr. Phys. **69**, 1936–1983 (2007). https://doi.org/10.1016/j.jastp.2007.08.010